# Can subduction initiation at a transform fault be spontaneous?

Diane Arcay [1], Serge Lallemand [1], Sarah Abecassis [1], and Fanny Garel [1]

[1]Geosciences Montpellier, Univ. Montpellier, CNRS, Univ. Antilles, Montpellier, France

**Correspondence:** D. Arcay (diane.arcay@umontpellier.fr)

**Abstract.** We propose a new exploration of the concept of "spontaneous" subduction, i.e., lithospheric gravitational collapse without any external forcing, at a transform fault (TF). We first seek candidates in recent subduction initiations at a TF that could fulfill the criteria of spontaneous subduction and retain 3 natural cases: Izu-Bonin-Mariana (IBM), Yap, and Matthew & Hunter. We next perform an extensive exploration of conditions allowing spontaneous gravitational sinking of the older plate in a oceanic TF using 2D thermo-mechanical simulations. Our parametric study aims at better deliminating the ranges of mechanical properties necessary to achieve the old plate sinking (OPS). The explored parameter set includes: crust and TF densities, brittle and ductile rheologies, and width of the weakened region around the TF. We focus on characterising OPS conditions in terms on (1) reasonable vs unrealistic values of mechanical parameters and (2) comparison to modern cases of subduction initiation in a TF setting. When modelled, OPS initiates following one of two distinct modes, depending mainly on the thickness of the overlying younger plate (YP). Asthenosphere may rise up to the surface above the sinking old plate provided that the YP remains motionless (verified for ages ≥5 Myr, mode 1). For lower YP ages (typically ≤2 Myr), the YP is dragged towards the OP resulting in a double-sided subduction (mode 2). When triggered, spontaneous OPS is extremely fast. The basic parameters to simulate OPS are the brittle properties of the shallow part of the lithosphere, controlling the plate resistance to bending, the distance away from the TF over which weakening is expected, and crust density. We find that all mechanical parameters have to be assigned extreme values to achieve OPS, that we consider as irrelevant. Furthermore, we point out inconsistencies between the processes and consequences of lithospheric instability as modelled in our experiments and geological observations of subduction infancy for the 3 natural candidates of subduction initiation by spontaneous OPS. We conclude that spontaneous instability of the thick OP at a TF evolving into mature subduction is an unlikely process of subduction initiation at modern Earth conditions.

## 1 Introduction

The process of spontaneous subduction deserves to be explored again following recent discoveries during Ocean Drilling Project 375 in the back-arc of the proto-Izu-Bonin subduction zone. The nature and age of the basaltic crust drilled there appeared to be similar to those of the forearc basalts (FAB) underlying the boninites of the present Izu-Bonin forearc (Hickey-

Vargas et al., 2018). The consequences of this discovery are controversial since they are supposed to support the concept of spontaneous subduction for some authors (Arculus et al., 2015; Stern and Gerya, 2018), whereas other authors do not (Keenan and Encarnación, 2016; Lallemand, 2016).

The notion of "spontaneous subduction" originates from two observations: (1) Uyeda and Kanamori (1979) first described the

5  Mariana-type extreme subduction mode where an old oceanic plate sunk, driven by its weight excess into a vertical slab in association with back-arc extension; (2) A few years later, in the early 1980s, Bonin Island volcanic rocks analysis and deep sea drilling (Leg 60) in the adjacent Izu-Bonin-Mariana (IBM) subduction zone forearc revealed rocks called boninites that combined the characteristics of arc-lavas and MORB (Natland and Tarney, 1981; Bloomer and Hawkins, 1983). A conceptual model was then proposed by Stern and Bloomer (1992) reconciling these observations in which an old plate may sink in the

10  mantle under its weight along the weak boundary formed by a transform fault. Numerical models (Hall and Gurnis, 2003; Gurnis et al., 2004) first failed to support this process of spontaneous subduction, and concluded that a tectonic force was required to initiate subduction. Later, they finally succeeded to simulate spontaneous subduction in specific contexts such as lithospheric collapse around a plume head (Whattam and Stern, 2015) or the conjunction of a large density contrast with a very weak fault zone between the adjacent lithospheres (Leng and Gurnis, 2015).

15  In this study, we will adopt the definition of Stern and Gerya (2018): spontaneous subduction is caused by forces originating at the subduction initiation site and not elsewhere (Fig. 1b). They define three different settings where spontaneous subduction may develop: passive margin, transform fault (TF) or plume head. The only Cenozoic examples that were attributed by Stern and Gerya to potential sites of spontaneous subduction initiation, i.e., IBM, and Tonga-Kermadec, correspond to the TF setting (Fig. 1a). In these two examples, the relics of the subduction initiation stage date back to Eocene and are thus subject to

20  controversy. We first recall the natural examples for which oceanic TFs or fracture zones (FZs) might have evolved into a subduction zone. Then, numerical models addressing subduction initiation processes in a similar context are analyzed before developing our own numerical approach. The range of parameters allowing spontaneous subduction initiation in our models will finally be compared with the reasonable values characterizing the natural processes.

## 1.1 From oceanic TF or FZ to subduction in nature

25  Table 1 and Fig. 1 summarize Cenozoic settings where oceanic TFs or FZs underwent deformation that sometimes evolved into subduction and other times not. The regions are classified in Table 1 such that the older plate (OP) underthrusts the younger in the first group (Fig. 1b,c,d, IBM, Yap, Matthew & Hunter, Mussau, Macquarie, Romanche), whereas the downgoing plate is the youngest in the second group (Fig. 1d,e, Hjort, Gagua, Barracuda, Tiburon) and finally those for which it appears to be impossible to determine the relative age of one plate with respect to the other at the time of initiation (Fig. 1f, Gorringe, St

30  Paul, Owen). The analysis of all these natural cases show that the 3D setting and far-field boundary conditions are likely to play a major role on subduction initiation and on the selected age (old/young) of the subducting plate. Earlier studies showed that compression prevailed in the upper plate at the time of initiation for most of them, while it is unknown for IBM and Yap. In these two regions, subduction started more than 20 Myr ago (Hegarty and Weissel, 1988; Ishizuka et al., 2011) but, soon after they initiated, they underwent one of the strongest episodes of subduction erosion on Earth (Natland and Tarney, 1981;
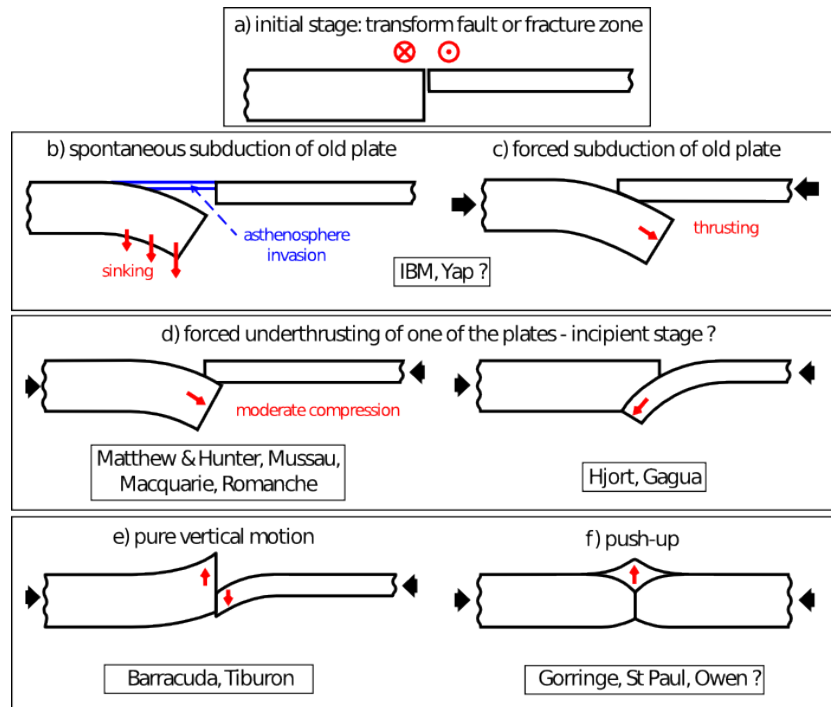
**Figure 1.** Various tectonic settings leading to vertical motion and/or convergence at transform plate boundaries, detailed in Table 1. Convergent black heavy arrows represent far field tectonic forces. Red light arrows outline the sense of motion of one plate with respect to the other. Red cross and dot in circles indicate transform motion. The thicker plate is the older one.

Hussong and Uyeda, 1981; Bloomer, 1983; Lallemand, 1995), so that all remnants of their forearc at the time of initiation were consumed (Lallemand, 2016). Geological evidences of the stress state at initiation are thus either subducted or deeply buried beneath the remnant Palau-Kyushu Ridge. So far, some authors (e.g. Ishizuka et al., 2018; Stern and Gerya, 2018) still argue that spreading, i.e. extension, occurred over a broad area from the back-arc to the forearc at the time of subduction

5  initiation. Back-arc extension concomitant with subduction initiation under compressive stress is compatible, as exemplified by the recent case of Matthew & Hunter at the southern termination of the New Hebrides subduction zone (Patriat et al., 2015, Fig. 1d). There, the authors suggest that the collision of the Loyalty Ridge with the New Hebrides Arc induced the fragmentation of the North Fiji Basin (Eissen spreading center & Monzier rift), whose extension yielded in turn a compressive stress along the southern end of the transform boundary (or STEP fault): accommodating the trench rollback of the New Hebrides Trench. It

10  is important to note that the geodynamic context of the Matthew & Hunter region is very similar to the one of the IBM proto-subduction (Deschamps and Lallemand, 2002, 2003; Patriat et al., 2015; Lallemand, 2016). Rifting and spreading in a direction normal to the TF has been documented at the time of subduction initiation. Since the conditions of spontaneous subduction do not require compressive stress, but the sinking of the oldest plate under its weight excess, and because of the lack of geological

records of what happened there, we consider that IBM and Yap subduction initiation might either be spontaneous (Fig. 1b), or forced (Fig. 1c). To decipher between these two hypotheses, we conduct a series of numerical simulations.

## 1.2 Modeling of spontaneous subduction initiation at a TF in previous studies

Numerical experiments showed that the old plate sinking (OPS) could spontaneously occur for a limited viscosity contrast between lithospheres and underlying asthenosphere (Matsumoto and Tomoda, 1983), in a model neglecting thermal effects. Still, without imposed convergence, subduction initiation failed when thermal diffusion was taken into account, even in the most favourable case of an old and thick plate facing a section of asthenosphere (Hall and Gurnis, 2003; Baes and Sobolev, 2017), unless the density offset at the TF was emphasised by including a thick and buoyant crust at the younger plate (YP) surface (Leng and Gurnis, 2015). In most cases of successful instability of the thick plate, lateral density contrasts at the TF are maximized by imposing at the TF an extremely thin younger plate (0 or 1 Myr old at the location where instability initiates) in front of a thicker plate whose age is chosen between 40 and 100 Myr, either in 2D (Nikolaeva et al., 2008) or 3D (Zhu et al., 2009, 2011; Zhou et al., 2018). For similar plage age pairs, Gerya et al. (2008) showed that successful spontaneous initiation requires the OP slab surface to be sufficiently lubricated and strongly weakened by metasomatism to decouple the 2 adjacent plates as plate sinking proceeds, while the dry mantle is assumed to be moderately resistant to bending. Assuming such "weak" rheological structure, OPS triggering occurs and results in an asthenosphere rise in the vicinity of the subduction hinge, which yields a fast spreading (from a few cm/yr to >1 m/yr). It has been described as a 'catastrophic' subduction initiation (Hall and Gurnis, 2003). This catastrophic aspect is hampered when thicker YP are considered (10 to 20 Myr old), crustal and mantle rheologies are less weak, and when shallow plate weakening develops progressively through time, e.g. by pore fluid pressure increase with sea water downward percolation in a low permeability matrix (Dymkova and Gerya, 2013).

These previous numerical studies helped unravel the conditions leading to OPS without any imposed external forcing. Still, recent incipient subduction zones the most likely to correspond to initiation by spontaneous sinking at a TF are not all associated with a significant plate age offset at the plate boundaries (Matthew & Hunter, Yap, Table 1). We thus propose a new investigation of the conditions of OPS to address the following 3 questions: What are the mechanical parameter ranges allowing OPS, especially for the TF settings the closest to spontaneous subduction conditions? Are these parameter ranges reasonable? Are the modeled kinetics and early deformation compatible with natural cases observations?

We choose a simplify set-up, without fluid percolation simulations and in 2D to allow a broad parameter exploration with an accurate numerical resolution.

## 2 Model set-up

### 2.1 Numerical code and boundary conditions

Models are performed using the Eulerian and finite element method developed by Christensen (1992). This thermo-chemical code of convection solves the momentum, energy, and mass conservation equations, assuming that rocks are incompressible,
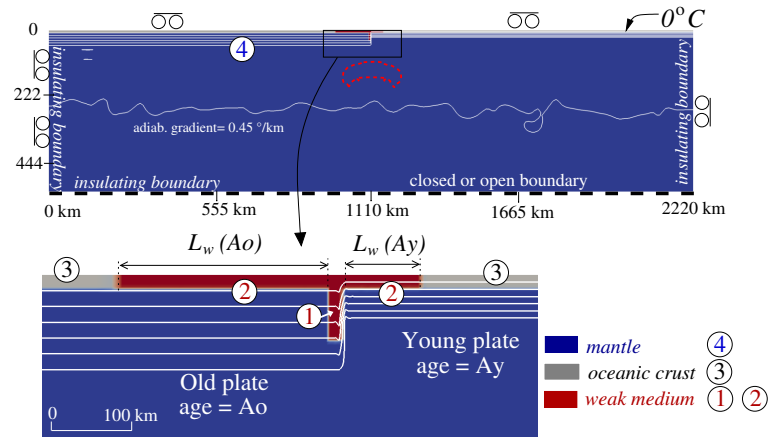
**Figure 2.** Boundary conditions, initial thermal state and material distribution at simulation start. One white isotherm every $200^oC$. If the box bottom is open, a vertical resistance against flow is imposed to simulate a viscosity jump about 10 times higher below the simulation box (Ribe and Christensen, 1994; Arcay, 2012). The red dotted line represents the hot thermal anomaly ($\Delta T = +250^oC$) imposed in some experiments. Bottom panel: close-up on the TF structure. The meaning of labels 1 to 4 is detailed in Sect. 2.4.

except for the thermal buoyancy term in the momentum equation, and for the adiabatic heating term in the energy equation (extended Boussinesq approximation). As shear heating has been shown to improve significantly strain localisation within the subduction interface (Doin and Henry, 2001; Thielmann and Kaus, 2012), it is included in the heat conservation equation, as well as a uniform heat production (Table 2). The simulation box, 2220 km wide and 555 km thick, is chosen to be large enough

5   to simulate convective interactions between shallow lithospheres and deep mantle (Fig. 2). The simulation box is discretised into $407 \times 119$ nodes. The resolution is refined in $x-$ and $z-$directions in the area encompassing the TF, i.e., between 966 km and 1380 km away from the left hand box side and for depths shallower than 124 km depth, where node spacings are set to 1.67 km. Outside the refined domain, node spacing is 10.5 km in both directions. The tracer density is uniform over the simulation box ($\sim 3.2$ per km$^2$), verifying that at least 9 tracers fill the smallest meshes. This numerical discretisation has been tested and

10  validated in a previous study (Arcay, 2017).

The original code has been adapted to allow the simulation of three different lithologies within the simulation box (Doin and Henry, 2001; Morency and Doin, 2004): mantle, oceanic crust, and a weak layer that would mimic an altered/hydrated and thence weakened region around a TF, with specific densities and rheologies (see Sect. 2.4). Composition is tracked by markers advected with the velocity field (van Keken et al., 1997). Slip is free at the surface and along vertical sides. We test the effect of

15  the box bottom condition, either closed and free-slip or open to mantle in- and outflows: It does not modify the future evolution of the fracture zone. Thermal boundaries conditions are depicted in Fig. 2.

## 2.2 Initial thermal structure

We investigate a wide range of lithosphere age pairs, the younger plate (YP) age, $A_y$, varying from 0 to 40 Myr, and the older plate (OP) age, $A_o$, from 5 to 150 Myr (Table 3), to cover optimally plate age ranges observed in nature (Table 1). The thickness of a lithosphere can be defined by the depth of the $1200^oC$ isotherm, $z_{LB}$, classically estimated (in m) using the

5   half-space cooling model (Turcotte and Schubert, 1982) by: $z_{LB} \sim 2.32\sqrt{\kappa A}$, where $\kappa$ is the thermal diffusivity (Table 2) and $A$ is the plate age in seconds. However, this thermal model overestimates a bit the oceanic lithosphere cooling and associated conductive thicknesses (Doin et al., 1996; Dumoulin et al., 2001; Hasterok, 2013). To correct simply this overcooling, we decrease lithospheric thicknesses predicted by Turcotte and Schubert by applying a factor set to 0.75, which allows to better match the modeled surface heat flows as a function of lithospheric ages. Between the surface and $z_{LB}$, the thermal gradient is

10  conductive and constant. The transform fault, located at the middle of the box top ($x =$1110 km), is modeled by a stair-step joining the isotherms of the adjacent lithospheres (Fig. 2). We test the effect of the TF thermal state, that should be cooled by conduction in the case of an inactive FZ, in a few simulations (Sect. 2.8).

Moreover, we test the possible influence of the asthenospheric structure at initiation, either uniform over the whole box or locally marked by thermal anomalies resulting from previous small-scale convection (Fig. 2). Results show that the process of

15  subduction initiation, in case of success or failure, does not depend on the average asthenospheric thermal structure. Still, in a few experiments, we impose at simulation start a thermal anomaly mimicking a small plume head ascending right below the TF, 200 km long and $\sim$75 km high, whose top is located 110 km depth at simulation start (Fig. 2). The plume thermal anomaly $\Delta T_{plume}$ is set to $250^oC$ (Table 3).

## 2.3 Rheology

20  We combine a pseudo-brittle rheology to a non-Newtonian ductile law. Pseudo-brittle rheology is modelled using a yield stress, $\tau_y$, increasing with depth, $z$:

$$\tau_y = C_0 + \gamma(C)\rho g z \tag{1}$$

where $C_0$ is the cohesive strength at the surface (Table 2), $\gamma$ is a function of composition $C$ (oceanic crust, mantle, or weak layer), $\rho$ is density, and $g$ is the gravity acceleration. The parameter $\gamma$ represents the yield strength increase with depth and can

25  be related to the coefficient of internal friction of the Coulomb-Navier criterion (Sect. 2.5). To simplify, we tag $\gamma$ as the brittle parameter. The brittle deviatoric strain rate is computed assuming the relationship: $\dot{\varepsilon} = \dot{\varepsilon}_{ref}(\tau/\tau_y)^{n_p}$, where $\dot{\varepsilon}$ is the second invariant of the deviatoric strain rate tensor, $\dot{\varepsilon}_{\text{ref}}$ is a reference strain rate and $n_p$ is a large exponent (Table 2): In the plastic domain, strain rates are close to zero if $\tau << \tau_y$ but become very large as soon as stress exceeds the yield stress $\tau_y$. Recalling that $\tau = \nu\dot{\varepsilon}$, the plastic viscosity, $\nu_b$, writes as:

30  $$\nu_b = \tau_y \frac{\dot{\varepsilon}^{\frac{1}{n_p}-1}}{\dot{\varepsilon}_{\text{ref}}^{\frac{1}{n_p}}} \tag{2}$$

A dislocation creep rheology is simulated using a non-Newtonian viscosity, $\nu_v$ defined by

$$\nu_d = B_0 \exp\left(\frac{E_a(C) + V_a \rho g z}{nRT}\right) \dot{\varepsilon}^{\frac{1}{n}-1} \qquad (3)$$

where $B_0$ is a pre-exponential factor, $E_a$ is the activation energy depending on composition $C$, $V_a$ is the activation volume, $n$ is the non-Newtonian exponent, $T$ is temperature, and $R$ is the ideal gas constant (Table 2). The effective viscosity, $\nu_{eff}$ is

5    computed assuming that the total deformation is the sum of brittle and ductile deformations.

## 2.4   Box composition and choice of parameters to test

The TF lithological structure is here simplified by considering only 3 different lithologies: the vertical layer forming the fault zone between the two oceanic lithospheres (label 1 in Fig. 2) and assumed to be the weakest material in the box, the oceanic crust (label 3), and the mantle (label 4). In all experiments, the Moho depth is set to 8.3 km for both oceanic lithospheres and

10    the width of the vertical weak zone forming the fault 1 is equal to 8.3 km. The depth of the weak vertical zone 1 depends on the chosen older plate age, $A_o$: It is adjusted to be a bit shallower than the OP base, by $\sim$15 to 30 km. Furthermore, we want to test the effect of the lateral extent of this weakening, outside the gouge fault, $L_w$ (label 2 in Fig. 2). Indeed, depending on the type of TF, the weak zone width may be limited to $\sim$8 km such as for the Discovery and Kane faults (Searle, 1983; Detrick and Purdy, 1980; Wolfson-Schwehr et al., 2014), implying $L_w =$0 km in our model, or on the contrary the weak zone

15    width may reach 20 to 30 km as for the Quebrada or Gofar TFs (Searle, 1983; Fox and Gallo, 1983): $L_w$ can thus be varied up to 22 km. In most experiments, we impose the same value for the lateral extent of crust weakening on both lithospheres: $L_w(A_o) = L_w(A_y)$, except in a few simulations.

To unravel the conditions allowing spontaneous subduction triggering, we test the influence of the physical properties of the different lithologies forming the TF area. We focus on 5 parameters: the brittle parameter for the oceanic crust, $\gamma_c$, and the one

20    for the mantle, $\gamma_m$, in the pseudo-brittle rheology (equation 2), both affecting the plate resistance to bending; the respective densities of the oceanic crust, $\rho_c$, and of the weak layer forming the interplate contact, $\rho_{TF}$, that either resist plate sinking if buoyant, or may promote it if dense; and finally the ductile strength imposed for the oceanic crust and the weak zone, tested by varying the activation energy $E_a^c$ (equation 3). The TF "gouge" labelled 1 is either made of oceanic crust ($\gamma_{TF} = 0.05$) or, in most experiments, filled with the weak material. In these cases, a very low brittle yield strength is assumed at the interplate

25    contact (Gurnis et al., 2004; Gerya et al., 2008): $\gamma_{TF} = 5 \times 10^{-4}$. When $\gamma_c = \gamma_{TF} = 5 \times 10^{-4}$, assuming that the weak layer and the oceanic crust are mechanically identical, the weak layer then entirely covers the whole plate surface: $L_w =$1100 km. Similarly, as the activation energy $E_a^c$ (eq. 3) is the same for the oceanic crust and the weak material, assuming a low ductile strength for the TF is equilavent to cover the whole plate surface by the weak layer ($L_w =$1100 km). In some experiments we replace the very weak layer filling the TF gouge by the more classical oceanic crust labelled 3 to test the effect of a stiffer fault.

30    In that case, $\gamma_{TF} = \gamma_c = 0.05$ and $L_w = 0$ km: the TF and both plate surfaces are made of gabbroic oceanic crust (Table 3).

### 2.5 Ranges of investigated physical properties

#### 2.5.1 Brittle properties for oceanic crust, TF and mantle lithologies

The brittle parameter $\gamma$ in equation 1 is related to the tectonic deviatoric stress, $\Delta\sigma_{xx}$, depending on lithostatic pressure, $\sigma_{zz}$ (Turcotte and Schubert, 1982): $\Delta\sigma_{xx} = \gamma\sigma_{zz}$. One may derive the relationship under compression between $\gamma$ and the classical

5  coefficient of static friction, $f_s$, defined by $f_s = \tau/\sigma_n$, where $\tau$ is the shear stress along the fault and $\sigma_n$ is the normal stress (Turcotte and Schubert, 1982):

$$\gamma = \frac{2f_s(1-\lambda)(1-\rho_w/\rho)}{\sqrt{1+f_s^2}-f_s} \qquad (4)$$

where $\lambda$ is the pore fluid pressure ratio and $\rho_w$ is the water density. The brittle parameter $\gamma$ moderately depends on the average density in the overlying column, $\rho$ (Fig. S1 . in the suppl. material). The internal friction coefficient, $f_s$, initially considered as

10  roughly constant ($f_s \sim 0.6$ to $0.85$, Byerlee, 1978) is suggested to vary with composition from recent experimental data. For a dry basalt, $f_s$ would be encompassed between 0.42 and 0.6 (Rocchi et al., 2003; Violay et al., 2012). Assuming high pore fluid pressure in the oceanic crust ($0.5 \leq \lambda \leq 0.9$), $\gamma_c$ from equation 4 is then close to 0.8 (Fig. S1). If the oceanic crust is altered by the formation of fibrous serpentine or lizardite, $f_s$ decreases to 0.30 (Tesei et al., 2018), entailing for a high pore fluid pressure ($\lambda = 0.9$) $\gamma_c \sim 0.05$, which we consider as the minimum realistic value for modelling the crustal brittle parameter (Fig. 3a). In

15  the presence of chrysotile, $f_s$ may even be reduced to 0.12 at low temperature and pressure (Moore et al., 2004), which would reduce $\gamma_c$ to $\sim 0.01$ (for $\lambda = 0.9$), deemed as the extreme minimum value for $\gamma_c$.

Regarding the TF, the fault material is assumed to be either mechanically similar to a weak serpentinized crust ($\gamma_{TF} = 0.05$) or even softer (e.g., Behn et al., 2002; Hall and Gurnis, 2005). In that case, we set $\gamma_{TF} = 5 \times 10^{-4}$.

At mantle depths, the pore fluid pressure ratio $\lambda$ is assumed to be zero, as the effect of pore fluid pressure on brittle strength is

20  more questionable than at crustal levels. The coefficient of internal friction for a dry mantle decreases from $f_s = 0.65$ (Byerlee, 1978) to $f_s \sim 0.35$ or 0.45 if peridotite is partly serpentinised (Raleigh and Paterson, 1965; Escartìn et al., 1997), leading to $\gamma_m$ between 1.6 and 0.8 for the most likely interval (Fig. 3b). The mantle brittle parameter $\gamma_m$ might decrease to $\sim 0.15$ ($f_s = 0.12$) if chrysotile is stable, which is nevertheless unexpected at mantle conditions. Lower $\gamma_m$ are considered as unrealistic, even if $\gamma_m = 0.02$ has been inferred to explain plate tectonic convection (still for a mantle devoid of a weak crustal layer, Korenaga,

25  2010).

#### 2.5.2 Crust and TF densities

The oceanic crust density is varied from the classical value for a wet gabbro composition in the pressure-temperature conditions prevailing at the surface (2920 kg.m$^{-3}$ Bousquet et al., 1997; Tetreault and Buiter, 2014). Crust density in the blueschist facies reaches 3160 kg.m$^{-3}$, but we try even higher densities, by imposing the mantle value, that would correspond to crust

30  eclogitization and the heaviest crust, to maximize the column weight within the older plate (OP) in order to promote its gravitational instability (Fig. 3c). Rocks forming the fault "gouge" are likely to be vertically highly variable in composition, possibly rich in buoyant phases such as serpentine and talc close to the surface (e.g., Cannat et al., 1991), and more depleted in
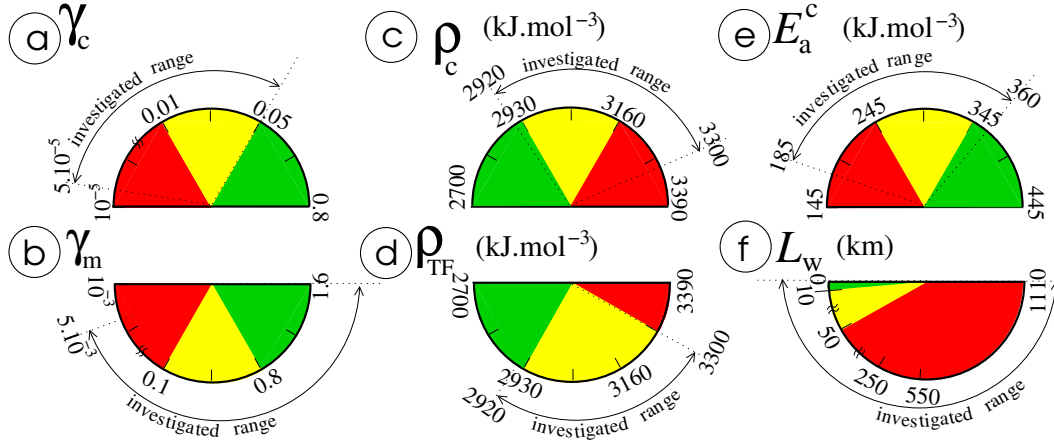
**Figure 3.** Physical properties tested in this study and investigated ranges. (a) Brittle parameter for the oceanic crust, $\gamma_c$; (b) Brittle parameter for the mantle, $\gamma_m$; (c) Oceanic crust density, $\rho_c$; (d) Density of the weak medium forming the TF, $\rho_{TF}$; (e) Activation energy of the oceanic crust, $E_a^c$, assuming that a non-Newtonian exponent $n = 3$ in eq. 3; (f) Lateral extent of the weak domain on both flanks of the TF, $L_{weak}$. Parameter intervals vary from realistic ranges (in green) to extreme values (in yellow). They are still extended beyond, up to unrealistic ranges to achieve the conditions allowing spontaneous subduction (in red).

hydrous phases at deeper level. Below the Moho, down to its deepest portion, the fault may be compounded of a mix between oceanic crust and altered mantle (Cannat et al., 1991; Escartìn and Cannat, 1999). The density of the fault gouge is thus likely to increase from the surface towards the deeper part of the fault, from a hydrated gabbro density to a mantle density. We thus test for $\rho_{TF}$ values spanning from a gabbroic density to a mantle one (Fig. 3d). Note that these densities correspond to reference values at surface conditions ($T = 0^o$C and $P = 0$ kbar), knowing that density is here a function of temperature through the coefficient of thermal expansion (Table 2).

### 2.5.3 Activation energy for the crust

From experimental estimates $E_a^{exp}$ for an oceanic crust composition, the most realistic interval for the crustal activation energy $E_a^c$ in this study can be defined by recalling that, as we use $n = 3$ in eq. 3, the equivalent activation energy must be computed as: $E_a^c = (n+1) \times E_a^{exp}/(n_e + 1)$, where $n_e$ is the experimentally defined power law exponent (Dumoulin et al., 1999). The activation energy $E_a^{exp}$ in the dislocation creep regime is encompassed between the one for a microgabbro, 497 kJ/mol (Wilks and Carter, 1990, with a non-Newtonian exponent $n_e = 3.4$ ) and the one of a dry diabase, i.e., 485±30 kJ/mol (Mackwell et al., 1998, with $n_e = 4.7\pm0.6$). For a basalt, $E_a^{exp}$ has been recently estimated to 456 kJ/mol (Violay et al., 2012, with $n_e \sim 3.6$). Lower values inferred for other lithologies are possible but less likely, such as for a wet diorite ($E_a^{exp} = 212$ kJ/mol, $n_e = 2.4$, Ranalli, 1995), and is used to define the lower bound of the "yellow" range for $E_a^c$ (Fig. 3e). A few experiments have shown that $E_a^{exp}$ can be as low as 132 kJ.mol$^{-1}$ ($n_e = 3$), if hornblende and plagioclase are present in high proportions (Yongsheng

et al., 2009). This activation energy, as well as the one of a wet quartzite ($E_a^{exp}$ =154 kJ/mol, $n_e = 2.3$, Ranalli, 1995), though used in numerous thermo-mechanical modellings of subduction, are considered as an unrealistic value in a TF setting. Still as a weakening process within the shallow lithosphere has been suggested to favor the older plate spontaneous sinking, we test in a set of experiments the effect of a very low crustal activation energy $E_a^c$, equal to 185 kJ.mol$^{-3}$ (Fig. 3e).

### 2.5.4 Distance from the TF of crust weakening

Regarding the lateral extent of the weak material, $L_w$, we test lengths in agreement with observed large or relatively small TFs ($L_w \leq$20 km, as described in the previous section) and increase it up to the extreme value of 50 km (Fig. 3f). Simulation results prompt us to perform experiments in which both lithospheres are entirely recovered by the weak layer ($L_w \sim$1110 km) to achieve the conditions of spontaneous subduction initiation.

Here, we first summarise experiments without OPS, then the simulations showing spontaneous gravitational instability of the OP. Next, we detail the effect of the different mechanical and geometrical parameters. Table 3 compiles the experiments explicitly quoted in the main paper. The exhaustive list of simulations performed in this study can be found in the Supplementary material (Table S1).

### 2.6 Overview of simulated behaviors other than OPS

We obtain numerous behaviors different from OPS, varying as a function of (1) the plate age pair ($A_y$,$A_o$), and, (2) the combination of densities, rheological parameters and of the weak layer lateral extent ($L_w$). This large simulation set summed up in Fig. 4 represents $\sim$65% of the 297 experiments performed in this study.

First, no tectonic deformation is modelled in a lot of experiments, i.e., deformation only occurs within the asthenosphere below the plates but is almost totally absent at shallower depths, where plate cooling takes place (Fig 4-1). This is notably obtained if the YP is too old, that is for $A_y \geq 3$ Myr up to 17 Myr depending on the physical parameter set (Fig. 6).

Second, we observe the YP ductile dismantlement, corresponding to a serie of several fast lithospheric drips, soon after simulation start (Fig 4-2), modelled when ductile strengths are low. The OP is not affected and solely cools through time.

Third, a transient retreat of the YP is modelled, in very few experiments, while the OP remains motionless (Fig 4-3). This occurs if the YP is very young ($A_y \leq 2$ Myr) and if the TF density, $\rho_{TF}$, is low (equal to the gabbro density). Because of its buoyancy, the weak material forming the TF rises up to the surface as soon as simulation starts. This fast vertical motion (velocities $\geq$50 cm/yr) is partly transmitted horizontally and deforms the weaker and younger plate, triggering a backwards motion. Velocities vanish as plate cooling proceeds.

Fourth, the gravitational instability of the YP is triggered in some models (Fig 4-4). The YP sinking occurs in a way very similar to the one expected for a thick plate spontaneous sinking (as sketched in Fig. 1). The polarity of the YP sinking depends on the density imposed for the TF interface ($\rho_{TF}$), and on whether (or not) the weak layer covers the YP surface ($L_w >0$ km). The duration of YP spontaneous sinking is always very brief ($<$0.5 Myr): either the process does not propagate fast enough to compete against plate cooling and strengthening (Fig 4-4b), or the diving YP segment is limited by the imposed length $L_w$ of lithosphere recovered by the weak material (Fig 4-4a).

Fifth, in some experiments of YP sinking, the OP also becomes unstable and starts sinking when a wider portion of weak and dense material ($L_w$ =50 km) is included (Fig 4-5). Still, the OP slab rapidly undergoes slab break-off once the $L_w$ long weak segment has been entirely subducted (Fig 4-5, 0.62 Myr), which we deem as too short to represent a successful OPS initiation. Sixth, subduction of the YP initiates at the TF when the TF material is as dense as the mantle, and vertically drags the YP into

5  the mantle (Fig 4-6). The motion can be transmitted away from the TF up to 500 km backwards, but, systematically entails a YP stretching at the surface as the slab is young and soft ($A_y \leq$7 Myr). This prevents subduction from lasting more than 1.5 Myr. Moreover, plate cooling frequently freezes the downward YP flow (Fig 5-6, bottom row).

In ∼40% of experiments showing OPS initiation, the process of subduction aborts very early, typically in less than ∼0.4 Myr (Fig 4-7), especially for OP older than 80 Myr . Velocities within the OP then vanish quite fast (Fig 4-7a). OPS also aborts

10  even when the mechanical decoupling does occur at the TF if hot mantle flows are too slow, and/or if the lateral extent of the weak material $L_w$ is narrow (Fig 4-7b).

## 2.7  Modes of OPS triggering

"Spontaneous subduction" is modelled when one of the two lithospheres is gravitationally unstable, which occurs if the total lateral density offset (vertically integrated) at the plate boundary is not balanced by plate, mantle, and TF resistance to defor-

15  mation. We observe spontaneous sinking of the OP for quite various pairs of lithosphere ages (Fig 5), that mostly depend on the chosen set of rheological parameters, and on the presence of the weak layer at the whole plate surface. When simulated, OPS occurs following one of two basic ways, later called mode 1 and mode 2. Mode 1 happens in roughly one half of OPS cases (Fig. 5a), and is the closest to the mechanism envisioned in the spontaneous subduction concept (Fig. 1b). The mantle flow generated by the OP sinking triggers an asthenospheric upwelling focusing along the weak TF "channel" up to the surface

20  ("asthenosphere invasion" in Fig. 1b), while the YP remains mostly motionless. The subduction process develops thanks to a fast hinge roll-back. As mantle velocities are huge, exceeding tens of m/yr in many cases, the asthenosphere catastrophically invades the box surface, filling a domain that is soon larger than 200 km, as depicted in Fig. 5a.

In mode 2, the asthenosphere invasion does not occur at the surface, and is often limited to the YP Moho. Mantle flow induced by OP bending drags the YP towards the OP (Fig. 5b, c). As a consequence, a significant mass of dense crust is transferred

25  from the top of the YP to the one of the OP, where the accumulated crust builds a crustal prism that loads the OP amplifying its bending and sinking. This phenomenon is observed in numerous cases, systematically if the YP age is 2 Myr (Table 3) and in several cases when $A_y$ is either 0 or 5 Myr (simulations S1a to S2b, S22j-k). In both initiation modes, velocities at slab extremity are very high (14.6 cm/yr in simulation S1a, 0vs2, up to ∼180 cm/yr in simulations S10a, 0vs80 and S11a, 0vs100). The duration to form a slab longer than ∼200 km is less than 1.5 Myr. The kinetics of the OPS process modelled in this study

30  is consequently always very fast. This swiftness very probably comes from the significant weakness that must be imposed in our modelling set-up to obtain the OPS triggering (see Sect. 2.8.2).
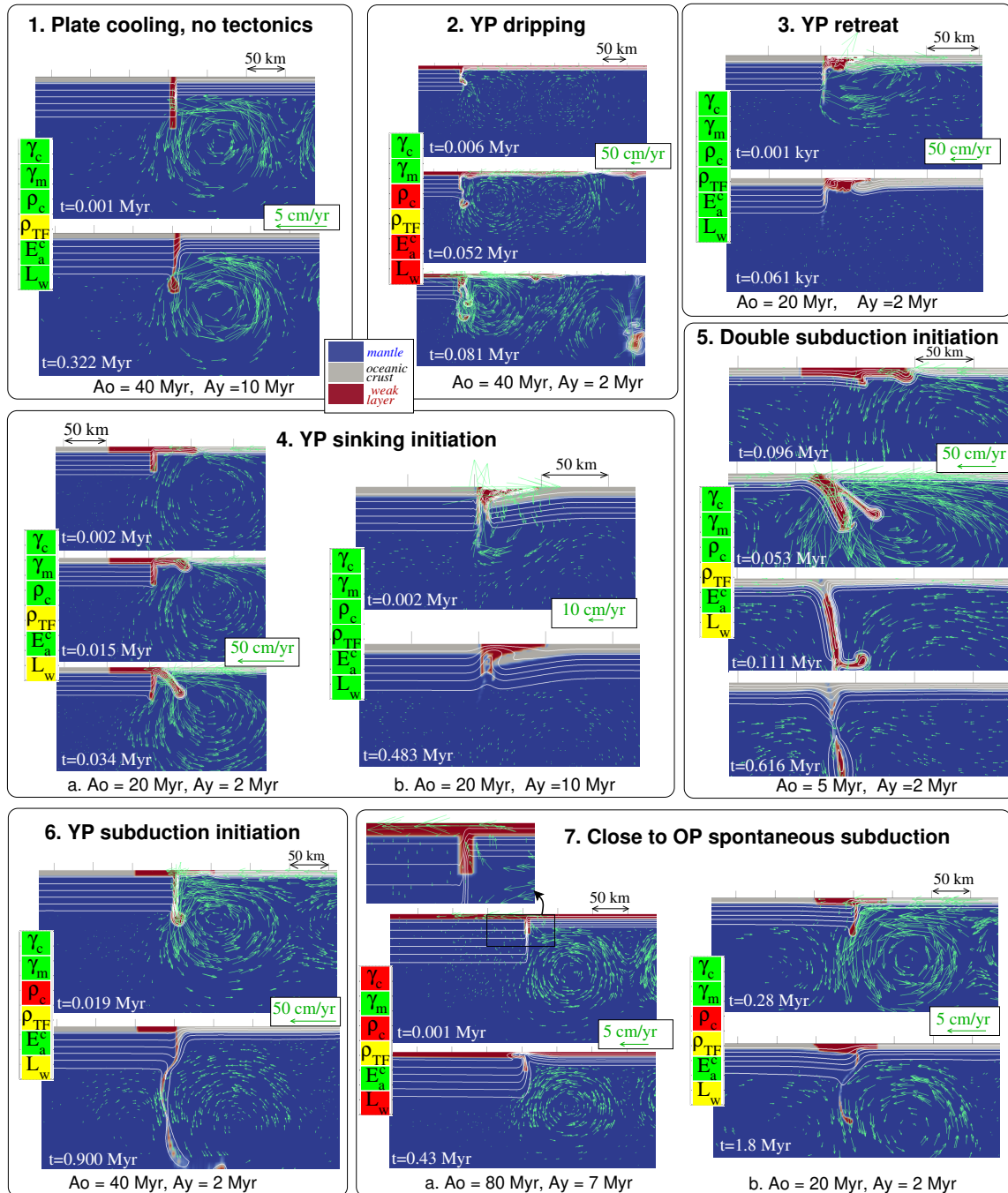
**Figure 4.** Illustration of the different simulated behaviors, OPS apart: close-up on the transform fault. (1) Absence of plate deformation (simulation S37x, Table 3). (2) Young plate dripping and dismantlement (simulation S17f). (3) YP retreat (simulation S16c). (4) Initiation of YP transient sinking (simulation S16b, panel a, and simulation S36b, panel b). (5) Simultaneous initiation of YP and OP sinkings (simulation S14n). (6) Initiation of YP vertical subduction at the TF (simulation S17o). (7) OP sinking initiation that soon aborts (simulation S34a, panel a, and simulation S16a, panel b). No vertical exaggeration. Velocity scale depicted in green is specific to each simulation. Parameter boxes are color-coded as a function of investigated ranges depicted in Fig. 3.
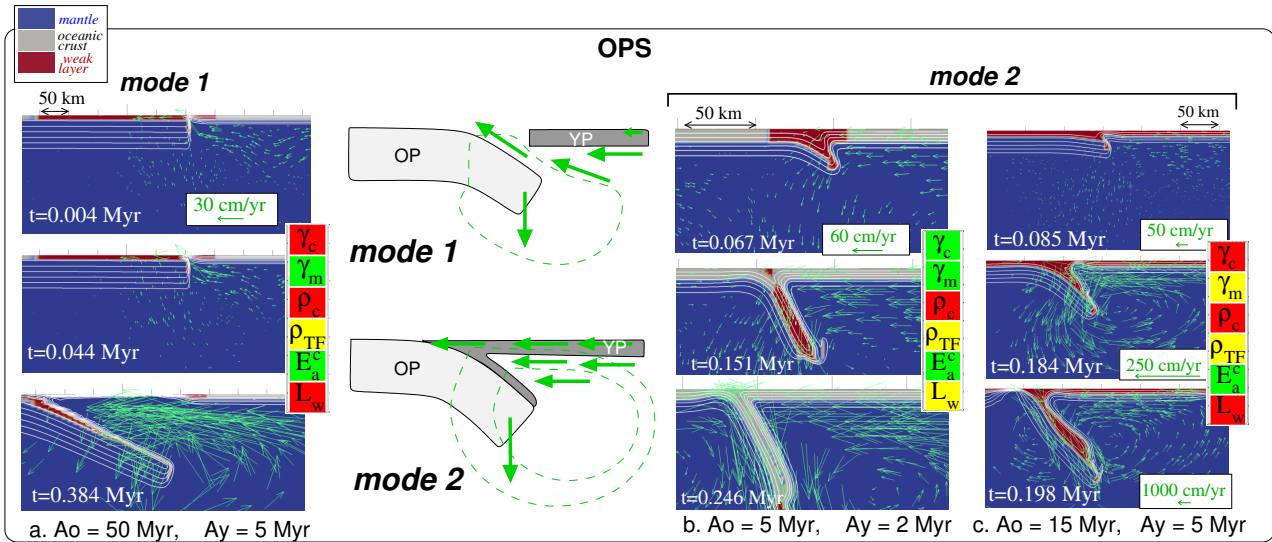
**Figure 5.** Illustration of OPS: mode 1 in simulation S27c (panel a), versus mode 2 in simulations S14i (panel b), and S22j (panel c). No vertical exaggeration. Parameter boxes are color-coded as a function of investigated ranges depicted in Fig. 3. Note that velocity scale in panel c is specific for each snapshot. Dashed lines in the middle sketch are a schematic outline of the stream function, while green arrows illustrate velocities.

## 2.8 Influence of tested parameters

Regime diagrams displayed as a function of the plate age pair $(A_y, A_o)$ sum up our main results obtained as a function of the assumed rheological set, density field, and the lithological distribution at the surface (oceanic crust vs. TF weak material, Fig. 6). These eight regime diagrams bring out the respective influence of the main physical parameters tested in this paper, specially for deciphering conditions allowing OPS. YP dismantlement, basically occurring when the ductile crust is softened, is not represented on regime diagrams (discussed at the end of the section).

### 2.8.1 TF and oceanic crust densities

Densities strongly affect the evolution of the TF system. If the TF weak medium is buoyant ($\rho_{TF} = \rho_c =$ 2920 kg.m$^{-3}$), the TF material rises up to the surface forming a small and localized buoyant diapir that pushes laterally on the younger lithosphere (Fig 4-3). The YP either shortens if it is weak enough ($A_y \leq$ 2 Myr, Fig. 6a) in a backward motion, or starts sinking if the YP thickness is intermediate ($2 < A_y <$ 20 Myr). On the other hand, a heavy material filling the TF gouge ($\rho_{TF} =$ 3300 kg.m$^{-3}$) inverts the aforementioned mechanics by pulling the YP downwards at the TF to form a vertical subduction (Fig. 4-6, labelled YPVSI for "YP vertical subduction initiation" in Table 3). Note that, when the fault density $\rho_{TF}$ is very high, the oceanic crust density, $\rho_c$, buoyant or not, does not actually affect the mode of YP deformation (compare diagrams 6b and d).
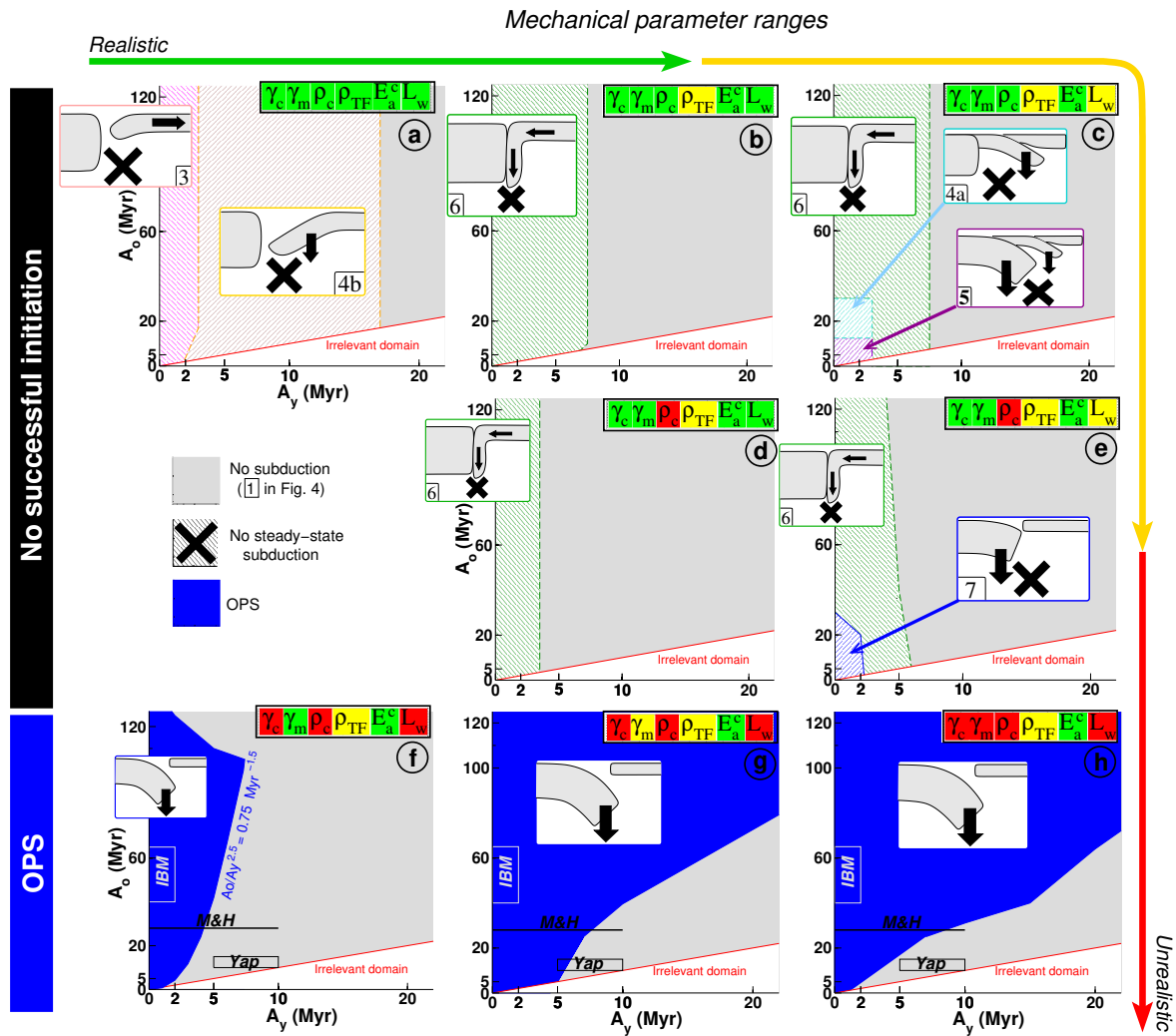
**Figure 6.** Regime diagrams as a function of the combination of rheological properties, densities, and TF weak domain extent, $L_w$. "Irrelevant domain" would correspond to cases where $A_y > A_o$. In hatched areas, only transient behaviors, lasting less than 0.5 Myr, are modelled. Inside inserted sketches, numbers refer to panel numbering in Fig. 4. Box colors correspond to parameter ranges depicted in Fig. 3. The parameter combination $\gamma_c$, $\gamma_m$, $\rho_c$, $\rho_{TF}$, $L_w$, is, respectively, in panel (a): 0.05, 1.6, 2920 kg.m$^{-3}$, 2920 kg.m$^{-3}$, 0 km; in panel (b) 0.05, 1.6, 2920 kg.m$^{-3}$, 3300 kg.m$^{-3}$, 0 km; in panel (c): 0.05, 1.6, 2920 kg.m$^{-3}$, 3300 kg.m$^{-3}$, 50 km; in panel (d): 0.05, 1.6, 3300 kg.m$^{-3}$, 3300 kg.m$^{-3}$, 0 km; in panel (e): 0.05, 1.6, 3300 kg.m$^{-3}$, 3300 kg.m$^{-3}$, 50 km; in panel (f): 5×10$^{-4}$, 1.6, 3300 kg.m$^{-3}$, 3300 kg.m$^{-3}$, 1100 km; in panel (g): 5×10$^{-4}$, 0.1, 3300 kg.m$^{-3}$, 3300 kg.m$^{-3}$, 1100 km; in panel (h): 5×10$^{-4}$, 0.05, 3300 kg.m$^{-3}$, 3300 kg.m$^{-3}$, 1100 km. In all panels, $E_a^c =$360 kJ/mol. In panel f, the boundary between "No subduction" and "OPS" domains corresponds to the relationship $A_o/A_y^{2.5} \gtrsim 0.75$ Myr$^{-1.5}$. When OPS is simulated (panels f to h), conditions in $A_o$-$A_y$ prevailing at subduction initiation inferred for Yap, IBM and Matthew & Hunter (Table 1) are superimposed on regime diagrams.

### 2.8.2 Lateral extent of the weak material

The aforementioned results are obtained when crust weakening is supposed to be localized at the TF only ($L_w$ =0 km). Assuming that crust weakening laterally spreads out away from the TF, the mode of YP vertical subduction switches to YP sinking by gravitational instability. This is observed when young plates are modelled on both sides of the TF ($A_y$ <5 Myr,

5 $A_o$ <40 Myr, Fig. 6c). The boundary between the dense weak material and the buoyant and stronger oceanic crust more or less acts as "secondary" plate boundary decoupling the 2 lithological parts of the YP, which does not occur if there is no buoyancy contrast between the crust and the weak material (Fig. 6e).

Moreover, we observe that enlarging the weak domain enables OPS in some cases if the YP is very thin ($A_y \leq 2$ Myr), whatever the oceanic crust density (Fig. 6c, e), although OPS fast aborts as OP subduction is limited to the weakened length $L_w$ (set to

10 50 km, Fig. 6e). Simulations show that OP sinking is enhanced if $L_w$ is much wider than expected in nature ($L_w \geq 50$ km, Fig. 3f, g, h). Otherwise, the backwards propagation of bending is hindered, which stops the OPS process. We conclude that a very wide area of crust weakening on both sides of the TF is a necessary condition to simulate OPS. We quantify more accurately for different pairs of plate ages the minimum length $L_w$ allowing a developed OPS in the Supplementary material (Sect. S2). These age pairs are selected in order to cover a wide range of YP age (2 to 20 Myr). We find that the domain of weakened crust

15 to impose in the vicinity of the TF is too large to be realistic, at least for classical mantle rheology, the only exception being the setting with a very thin YP ( $A_y$ =2 Myr). These results suggest the strong resistant character of thick YP on OPS triggering.

### 2.8.3 Crust brittle strength

What is the threshold in crust weakening enabling OPS? An usual value of the crust brittle parameter ($\gamma_c$ =0.05) does not allow OPS (Fig. 6a to e). Our simulations show that, if $\gamma_c$ is 100 times lower ($\gamma_c = 5 \times 10^{-4}$), OPS can initiate for numerous plate

20 age pairs (Fig. 6f), but such brittle parameter seems unrealistic. To determine the threshold in $\gamma_c$ allowing OPS, we choose a high plate age offset, 2vs80, the most propitious for OPS. We find out that the threshold in $\gamma_c$ is encompassed between $10^{-3}$ and $5 \times 10^{-3}$ (simulations S18a, b, c, d, e), still less than the lower bound of acceptable $\gamma_c$ ranges (Fig. 3a). We hypothesize that, for a small plate age offset, the threshold in $\gamma_c$ would have to be even lowered to observe OPS triggering.

### 2.8.4 Plate bending and mantle brittle parameter

25 Surprisingly, a very low crust brittle parameter is not sufficient to simulate OPS for some large plate age offsets, such as for $(A_y, A_o)$=10vs100 or 5vs120 (simulations S41a and S29a, Table 3, Fig. 6f). A mechanism is thus hindering OPS. We assume that thick OP are too strong to allow bending. We test it by reducing the mantle brittle parameter, $\gamma_m$, that affects in our brittle-viscous rheology the maximum lithospheric stress, from 1.6 (Fig. 6f) to 0.1 (Fig. 6g) and 0.05 (Fig. 6h). The domain of plate age pair where OPS can occur is then greatly enlarged towards much lower plate age offsets. We note that in most experiments

30 showing "mantle weakening"-induced OPS, OPS stops by an early slab break-off, once the infant slab reaches 200 to 300 km length, because the reduced slab strength cannot sustain a significant slab pull (Fig 5c).

In a limited set of experiments, we determine the threshold in $\gamma_m^{crit}$ below which OPS occurs. This threshold depends on the

OP age: $\gamma_m^{crit} \sim$0.06 for the plate age pair 10vs40 (simulations S37c to f), but the threshold is higher ($\gamma_m^{crit} \geq$0.1) for the plate age pair 10vs50 (sim. S38a). The thicker the OP, the easier the OPS triggering, as one may expect. We next compare experiments in which the OP and the YP are both progressively thickened, by considering the age pairs: 10v50 (sim. S38a), 15vs60 (S47a), 20vs80 (S51b-c), and 25vs100 (S57a-b), respectively. Experiments show that $\gamma_m^{crit}$ is: $\geq 0.1$, $\geq$0.1, $\sim$0.07, and
5  $\sim$0.06, respectively. Hence, the plate rigidity has to be reduced as YP thickness increases, despite the joint OP thickening, down to extremely weak $\gamma_m$ ranges ($\gamma_m^{crit} \ll 0.1$, Fig 3). In spite of the driving influence of thicker OP, thickening the YP impedes OPS in a much stronger way. Moreover, we find that lowering the OP rigidity by decreasing the mantle ductile strength (by lowering the activation energy $E_a^m$, Table 2) instead of the mantle brittle one ($\gamma_m$) is much more inefficient to obtain OPS (Table S1). Finally, our results suggest that the factors the resistance to OPS mainly comes from on OP flexural
10  rigidity and YP thickness and stiffness, in agreement with previous studies (Nikolaeva et al., 2010; Zhou et al., 2018).

### 2.8.5  Ductile strength decrease and plume-like thermal anomaly

The main effect of imposing a decrease in the crust and TF ductile strength (lowering $E_a^c$ to 185 kJ/mol) is to trigger the YP fast dismantlement by lithosphere dripping if the YP is young ($A_y =$2 Myr, Fig. 4-2). Otherwise a low $E_a^c$ has no effect on the two plates' deformation. One exception appears in simulation S14e, in which the weak ductile strength triggers mode
15  2-OPS. In this particular set-up, both lithospheres are very thin (($A_y, A_o$) =2vs5), and could be considered as "crustal" plates because the mantle lithosphere is very thin or almost absent. In this simulation the YP strength profile is actually similar to the other cases yielding mode 2-OPS (see Sect. S4 in the Supple. material), which should explain why decreasing $E_a^c$ allows OPS in this unique case. The YP destabilization and dripping result from the high crust density ($\rho_c =$3300 kg.m$^{-3}$) assumed in experiments performed with a reduced $E_a^c$. Indeed in experiments using an usual crustal density ($\rho_c =$2920 kg.m$^{-3}$), YP
20  vertical subduction is obtained instead (simulation S15g, 2vs10, for instance).
The thermal anomaly simulating an ascending plume head below the TF produces effects very similar to those of a reduced $E_a^c$: no effect if plates are older than 2 Myr, YP dismantlement if $A_y =$2 Myr and if the crust is dense ($\rho_c =$3300 kg.m$^{-3}$). Otherwise, for a normal crust density, a short stage of YP vertical subduction occurs after plume impact (2vs10, simulation S15h). The hot thermal anomaly never trigger OPS in this modelling.

25  ### 2.8.6  Additional tests on OPS conditions: TF gouge strength and width, TF vs fracture zones, and asthenosphere viscosity

We sum up in this section extra experiments performed to precise the mechanisms involved in OPS triggering. Detailed results are described in Sect. S3 in the Supplementary material. We first test the necessity of the fault softness to simulate OPS, by inverting the oceanic crust and TF respective brittle parameter ($\gamma_{TF} =$0.05, while $\gamma_c =$0.0005), and find that a very low TF
30  strength is critical to model OPS.
We next wonder if OPS (when not modelled) could be triggered by widening the fault gouge from the surface to the bottom of the fault (domain 1 in Fig. 2), by setting the fault width to 20 km instead of 8.3 km. Simulations show that OPS still does not occur, even if the mechanical decoupling is maximized ($\gamma_{TF}$ decreased to $5\times10^{-5}$). The mechanical interplate decoupling is

hence not sufficient alone to trigger OPS.

Subsequently, we investigate the possible role of the TF thermal structure. The interplate domain is assumed to be very thin, and modeled by a stair-step (Sect. 2.2). In nature this set-up would correspond to an active transform fault. If the fault is instead inactive (fracture zone), the thermal state of the plate boundary is likely to be cooled by thermal conduction, possibly stronger

5  and more resistant to plate decoupling. We test the effect of the TF thermal structure for the 2 plate age pairs for which OPS is simulated when crust weakening is assumed ($\gamma_c$ =0.0005), by widening the TF thermal transition (from 11 km up to 70 km), keeping the weak material forming the fault gouge at the center of the thermal transition in all cases. All these experiments show OPS. We here verify that the fault gouge weakening, governed by the soft material brittle properties, is independent of temperature, and at first order independent of the fault activity in our 2D set-up.

10  We finally test if a decrease in asthenosphere strength could help OPS triggering, by unbalancing the OP weight excess. Experiments show that asthenospheric velocities and OP deformation are slightly amplified but still not enough to trigger OPS.

## 3   Analysis: Mechanism and conditions of OPS triggering

### 3.1   OPS mode 1 vs mode 2

Velocity fields show that modes 1 and 2 differ by the resulting YP kinematics. When mode 1 occurs, the YP remains almost

15  motionless with respect to underlying asthenospheric flows (speeds ≤1 cm/yr and ≥ 20 cm/yr respectively, see Supplementary material Fig. S4). On the contrary, velocities during mode 2 are closer between the YP and the asthenosphere where speeds are high (between 25 and 100 cm/yr). Moreover, within the set of simulations showing OPS (Sect. 2.7), we find that mode 2 occurs in simulations where the YP age is 2 Myr, for various rheological sets, or if $A_y$ =5 Myr, provided that the mantle brittle strength is reduced. In all these experiments, the strength of the YP bottom part is the closest to the asthenospheric one

20  (viscosity ratios $\lesssim 10^2$ to $10^3$, Fig. S5 in the Supple. material). In contrast, the focusing of asthenosphere flows towards the weak TF is observed when the viscosity offset between the YP and the underlying mantle exceeds $10^2$. We hypothesize that mode 2 results from a strong coupling between the YP and the asthenosphere. The particular (though not meaningful) case of $A_y = 0$ Myr is addressed in the Supplementary material (Sect. S4).

The mode 2-OPS may be envisioned as an assymetric double-sided subduction (Gerya et al., 2008, see the sketch in Fig. 5).

25  In this subduction mode, the thick OP sinking drives the YP downward flow at the slab surface, because plate decoupling at shallow levels does not occur. In mode 1, asthenosphic flows related to OPS cannot drag the YP. The asthenosphere upwelling along the TF results from the need to decouple the 2 plates' motion to enable OP downwelling and hinge retreat whereas the YP is almost motionless. In mode 2 this shallow interplate decoupling is not required since the YP is easily dragged by asthenosphere. Simulations by Gerya et al. (2008) suggest that the thick OP lubrication by metasomatism is a way to force

30  plate decoupling to model one-sided subduction.

### 3.2 Plate ages allowing OPS

The boundary between OPS and absence of subduction can be defined for an usual mantle brittle parameter $\gamma_m = 1.6$ (Fig. 6f) using simulations in which OPS aborts (such as simulations S25a, 5v35; S29a, 5v120, or S34a, 7vs80). We observe a dichotomy in the OPS domain boundaries. On the one hand, for thick OP ($A_o >$ 100 Myr), OPS is prevented if the YP is not

5   extremely thin (plate age younger than 5 Myr). On the other hand, for thinner OP ($A_o \leq$ 100 Myr), we experimentally show that the OPS condition corresponds to the relationship: $A_o/A_y^{2.5} \gtrsim 0.75$ Myr$^{-1.5}$ (Fig. 6f). In both cases, the influence of $A_y$ is either strong or predominant. The YP age is the major determining factor in the TF evolution, compared to the OP age (considering apart the cases where the mantle brittle strength is reduced), which confirms the conclusion derived in Sect. 2.8.4 on the highly resistant effect of the YP thickness. This hindering effect results from two processes. On the one hand, high $A_y$

10  ages yield low pressure gradients across the TF, due to a density contrast that decreases with YP ageing (e.g., Hall and Gurnis, 2003). On the other hand, YP ageing increases the YP strength competing against asthenosphere upwelling in the vicinity of the TF in OPS mode 1. As a result, the most propitious conditions for OPS correspond to TFs where the thinner lithosphere is as young as possible.

### 3.3 Parameters resisting and promoting OPS

15  OPS is triggered if pressure gradients at the TF related to density offset exceeds plates and mantle resistance to deformation. Density contrasts are maximized when the YP is thin, which partly explains the dominant role of the age of the YP ("proto-overriding" plate), compared to $A_o$, on subduction initiation, as already underlined in other studies (Nikolaeva et al., 2010; Dymkova and Gerya, 2013). Our results show that plate instability is essentially promoted by three mechanical conditions: when low brittle strengths are assumed for (1) the oceanic crust and (2) the mantle, and (3) if the TF allows plate decoupling.

20  A weak brittle crust (1) enhances fast propagation of deformation at shallow depths, that cannot be obtained in our modelling by crust ductile softening (contrary to Nikolaeva et al., 2010, in a passive margin set-up). Moreover, the lowering of the crust brittle strength must be developed far away from the TF to allow OPS. Although the minimum spatial scale of crust softening depends on plate age pair, we find that it is generally of the order of a hundred(s) of km. One may argue that the necessity of decoupling propagation close to the surface by shallow softening is related in our modelling to the absence of free surface.

25  However, models including either a free surface or a "sticky air" layer (Nikolaeva et al., 2010; Marques and Kaus, 2016) show a very similar kinematics, with very close characteristic time scales for rheologies comparable to ours (Sect. 3.4). This confirms the results from Quinquis et al. (2011) showing that a free-slip model can well reproduce the subduction dynamics simulated with a free surface method as long as a shallow weak (crustal) layer is included. Low brittle mantle strength (2) strongly promotes not only the OP plate bending and sinking, by limiting the plate flexural rigidity, but also YP deformations close to

30  the plate boundary where asthenosphere upwelling focuses in mode 1. At last, the TF must also be weak to enable mechanical decoupling between neighboring plates (3).

The amplitude of the preceeding processes is regulated by the 6 physical parameters investigated in this study (Fig. 3). Plainly,

OPS cannot be simulated for a realistic set of physical parameters (Fig. 6a). To achieve OPS, the cursors controlling plate mechanical structures have been tuned beyond reasonable values (Fig. 6f to h).

### 3.4 Initiation swiftness and influence of elastic rheology

In a TF or fracture zone numerical setting without any external forcing, if subduction initiation has to occur it can only take place at simulation onset, because plate cooling first implies a fast stiffening of oceanic lithospheres and second quickly attenuates the plate density offset (Hall and Gurnis, 2003). The process of subduction initiation modelled in our study systematically occurs very briefly after simulation start, in less than 1 to 1.5 Myr. This quite 'catastrophic' way of initiation has been also simulated in less than 0.8 Myr for other tectonic settings or triggering modes, such as passive margins (Nikolaeva et al., 2010; Marques and Kaus, 2016) or plume-induced mantle flows (Lu et al., 2015), using rheological conditions very close to the ones assumed in this study. The initiation process is slightly slowed down but remains fast (duration < 3 Myr) when the necessary weakness of the plate stronger part is not fully imposed at simulation onset but progressively develops, thanks to damaging or water-related weakening effects (Hall and Gurnis, 2003; Gurnis et al., 2004; Gerya et al., 2008; Dymkova and Gerya, 2013). In addition, by neglecting elastic deformation, the amount of plate and interplate weakening required to trigger OPS may be excessive (Farrington et al., 2014). Including elasticity would likely slow down a bit OPS initiation by limiting the threshold in strength contrast, but the incipient subduction has been shown to remain 'catastrophically' fast (Hall and Gurnis, 2003). Besides, previous modelling of subduction initiation including elasticity showed that the elastic flexure was a basic term of the subduction force balance (Hall and Gurnis, 2003; Gurnis et al., 2004), that is replaced in our model by the viscous (and brittle) resistance to bending, as in numerous approaches of subduction that successfully reproduce topographies, strain and stress patterns observed in natural cases (e.g., Billen and Gurnis, 2005; Buffett, 2006).

## 4 Discussion

### 4.1 Model limitations

Subduction initiation at a TF is here simplified by a 2D process whereas the fault strike-slip basically implies that it takes place as a 3D phenomenon. For instance, the setting of Matthew & Hunter used to be a subduction-transform edge propagator ('STEP') fault 2 Myr ago (Patriat et al., 2015), where 3D mantle flows associated with the Australian plate subduction likely affected the TF structure and evolution, possibly favouring subduction initiation. This case exemplified the role of 3D far-field tectonics during subduction infancy (Table 1), and the potential role of deep mantle flows. Upward and downward mantle flows, even far away from the initiation site, have be shown to be able to initiate subduction in 2D models (Lu et al., 2015; Baes and Sobolev, 2017). On the other hand, studies in 3D by Boutelier and Beckett (2018); Zhou et al. (2018) showed that subduction initiation depends on along-strike variations in plate structure. However the strike-slip kinematics of an active TF has up to now, to our knowledge, never been taken into account in subduction initiation simulations. We show that a TF thermal state cooler than modelled by a stair-step does not hinder OPS. However, our results verify that in 2D, without simulating the TF

strike-slip, the process of spontaneous OPS has to occur at simulation onset, to avoid the impeding effect of plate stiffening with further conductive cooling. Including in 3D experiments the TF motion would compete against this strengthening effect in the area nearby the active spreading center.

Regarding fluid transfers and fluid-related weakening effects, we indirectly account for mantle weakening by the formation of stable mechanically weak hydrated phases (such as talc or serpentine minerals) by lowering the mantle brittle parameter as a function of assumed stable hydrous phases (Sect. 2.5.1). Dymkova and Gerya (2013) show that deep fracturation during early OP deformation and percolation of sea water down to ∼25 km depth can enable the thick plate bending, assuming low porosity ($\leq$2.5%) and low mantle matrix permeability ($10^{-21}$ m$^2$) to significantly increase pore fluid pressure. In our approach a high pore fluid pressure ratio ($\lambda >$0.5) would imply a low mantle brittle parameter ($\gamma_m <$1, Fig. S1 in the supporting information) for which OPS is modelled for a broad ranges of plate ages (see for instance diagrams 6g-h), in agreement with Dymkova and Gerya's results. However the low permeabilities assumed by Dymkova and Gerya (2013) are questioned by recent experiments of mantle hydration at ridge or water percolation in a peridotite, and by estimates from a peridotite aquifer (Godard et al., 2013; Farough et al., 2016; Dewandel et al., 2004). These studies rather infer permeabilities encompassed between $10^{-19}$ and $10^{-16}$ m$^2$, that would hamper high pore fluid pressures and eventually, plate bending.

## 4.2 Comparison between OPS model requirements and natural cases

When analyzing the results of our parametric study (Sect. 3), the striking conclusion is that none of the realistic sets of parameters allowed spontaneous subduction. Figure 6f,g,h shows that, even if one of the plates is extremely young ($<$ 7 Myr), the oceanic crust should be very dense ($\rho_c = 3300$ kg.m$^{-3}$) as well as drastically weakened ($\gamma_c = 5 \times 10^{-4}$) at considerable distances from the TF ($L_w \gg$50 km), to satisfy OPS necessary conditions. Assuming - as an exercice - that such extreme conditions were fulfilled, OPS must develop (1) at simulation onset before plates cooling so that gravitational instability is maximal and (2) catastrophically in terms of kinetics of the process with sinking rates $\geq$ 15 cm/yr, up to 180 cm/yr.

As depicted in Sect. 1, only two natural cases: IBM & Yap, attest for subduction initiation of an old oceanic plate beneath a young one at a TF, which later evolved into a mature subduction during the Cenozoic. The range of ages for both plates at time of initiation (Table 1) has been plotted in Fig. 6 f,g,h. Plate ages at Yap subduction initiation are incompatible with the conditions of OPS inferred from our modelling results, suggesting that spontaneous subduction of the thicker plate is highly unlikely. Only IBM falls into the OPS domain based on age pairs at onset. There, the initial state of stress being unknown, as both plates edges have been consumed in subduction, it begs the question as to whether the old Pacific plate sunk spontaneously. Now the question is: to which extent the rheological parameters and the characteristics of subduction initiation were satisfied? Beyond the unrealistic values of crustal densities and brittle properties, the expected sinking rates and asthenosphere rise are great. The slab typically reaches 200 km length within ∼1 Myr, so that remnants of the resulting "forearc crust" should be restricted to a very short time span. The argument of Arculus et al. (2015) that new findings of juvenile 52-48 Myr old oceanic crust in the Amami-Sankaku Basin, far away from those already found in the IBM forearc (so-called FABs), confirming the spontaneity of the subduction initiation and wide extent of the asthenosphere invasion, was refuted by Keenan and Encarnación (2016) since younger juvenile oceanic crust cannot be used as a test for early uplift in pre-subduction initiation basement rocks.

A second argument comes from the boninitic nature of the primary embryonic arc combining MORB and slab-derived hydrous fluid signatures (Ishizuka et al., 2006). Those boninites erupted between 51 and 44 Ma in the Bonin present arc and forearc (Ishizuka et al., 2011; Reagan et al., 2019) and between 48 and 43 Ma in the Mariana present forearc (Johnson et al., 2014). This time span appears incompatible with the swiftness of the processes required in our models. An alternative geodynamic scenario satisfying both the magmatic and the tectonic constraints has been proposed by Lallemand (2016). The kinematic change of Pacific plate motion following the Izanagi slab break-off around 60-55 Ma (Seton et al., 2015) created enabling conditions for convergence across a major TF or FZ. Compressive deformation progressively localized until subduction starts around 52 Ma. At about the same time, the occurrence of the Oki-Daito plume has produced the splitting of the remnant arcs brought by the younger plate (Ishizuka et al., 2013). Oceanic basalts, further called FABs, spreaded along axes perpendicular to the nascent trench (Deschamps and Lallemand, 2002, 2003). Boninites erupted as soon as hydrous fluids from the subducting plate metasomatized the shallow asthenosphere beneath the newly formed oceanic crust. Later, tectonic erosion along the IBM trench removed the frontal 200 km of the upper plate, exposing in the present forearc basalts and arc volcanics initially formed far from the trench.

As observed along the Hjort trench, subduction may start as soon as compressive tectonic forces are applied across a TF, but one should note that the subducting plate is the youngest there (Table 1, Abecassis et al., 2016). IBM and Yap cases probably fall in this "forced" category as mentioned above but we lack of direct field evidences as they were both deeply eroded along their overriding edge.

### 4.3 OPS failure is not excluded

Among the numerous parameter values tested in this study, especially those within reasonable (green) ranges, we have observed that most of them led to incipient subduction of either the young or the old plate but failed soon after (Fig. 6a to e). We have compiled in Table 1 several cases of potential subduction initiation along TFs or fracture zones that either failed (Romanche, Gagua, Barracuda, Tiburon, Gorringe, Saint Paul, Owen) or just initiate so that we still ignore how it will evolve (Matthew & Hunter, Mussau, Macquarie). The advantage of studying the aborted cases is that we still have access to the deformation which accompanied subduction initiation and compression was always recorded in the early stages (see references in Table 1 caption). These incipient subduction areas are either restraining bends along transform faults or underwent changes in plate kinematics from strike-slip to transpression. A major limiting factor is the cooling of adjacent plates, as the distance from the spreading center or the plume increases, inhibiting their flexural capacities.

### 5 Conclusions

We perform a large set of 2D thermo-mechanical simulations to study the conditions of spontaneous sinking of the older plate at a TF, by investigating broad intervals of plate ages and by paying special attention to the mechanical parameter ranges allowing OPS. OPS is simulated notably if the oceanic crust is dense and mechanically soft far away from the TF, on both sides of the plate boundary. Our results confirms that the OP resistance to bending and the YP thickness are the factors the

most significant preventing OPS. Reducing the brittle properties of the oceanic lithosphere is thus the most efficient way to trigger OPS, compared to a softening by lowering the ductile strength, imposing a hot thermal anomaly, or reducing the asthenospheric viscosity. When these extreme conditions are imposed, two processes of OPS are obtained, depending mainly on the assumed YP thickness. They can be summed up as (1) an OP rapid sinking decoupled from the YP kinematics, associated

5   with a significant rise of asthenosphere towards the subducting slab hinge, and (2) a dragging of the YP by the sinking OP that is considered as a 2-sided subduction mode. In all cases, whatever the mode, OPS occurs in less than 1.5 Myr, that is, in a extremely short time span, and only if the initial mechanical set-up is adjusted beyond reasonable limits. From the parametric study we conclude that OPS cannot be simulated for a realistic combination of mechanical parameters. By comparing our modeling results to the most likely natural cases where spontaneous subduction at a TF has been invoked, we find that even

10   though extreme mechanical conditions were assumed, the plate age setting at Yap should prevent OPS. Regarding the case of Izu-Bonin-Mariana, the kinetics of subduction initiation evidenced by geological records is not compatible with the catastrophic mode systematically simulated in our experiments. We finally conclude that spontaneous instability of the thick OP at a TF is an unlikely process of subduction initiation at modern Earth conditions.

*Author contributions.*   DA and SL designed the experiments and DA and SA carried them out. DA, SL and FG carried out the analysis and

15   interpretation of simulation results. DA and SL prepared the manuscript with contributions from FG.

*Competing interests.*   The authors declare that they have no conflict of interest.

*Acknowledgements.*   Yann Heurtebize is acknowledged for his preliminary studies, during his Master degree in 2016, exploring the processes of OP subduction. This study benefited from stimulating discussions about TF properties and evolution with M. Ligi, M. Maia, D. Brunelli, M. Godard, and M. Patriat. We are grateful to Stéphane Arnal, Fabrice Grosbeau, and Josiane Tack for the maintenance and development of

20   the lab cluster of computing nodes on which all numerical experiments were performed. We are also grateful to Anne Delplanque who drew Fig. 1. This study was supported by the CNRS-INSU (National Institute of Universe Science) program "TelluS-SYSTER" (2015 and 2016).

# References

Abecassis, S., Arcay, D., and Lallemand, S.: Subduction initiation at fracture zones : conditions and various modes, in: abstracts of the GeoMod conference, Oct. 17-20, p. 14, La Grande Motte, France, http://geomod2016.gm.univ-montp2.fr/Home.html, 2016.

Arcay, D.: Dynamics of interplate domain in subduction zones: influence of rheological parameters and subducting plate age, Solid Earth, 3, 467–488, https://doi.org/10.5194/se-3-467-2012, http://www.solid-earth.net/3/467/2012/, 2012.

Arcay, D.: Modelling the interplate domain in thermo-mechanical simulations of subduction: Critical effects of resolution and rheology, and consequences on wet mantle melting, Phys. Earth Planet. Inter., 269, 112–132, https://doi.org/10.1016/j.pepi.2017.05.008, https://doi.org/10.1016/j.pepi.2017.05.008, doi:10.1016/j.pepi.2017.05.008, 2017.

Arculus, R. J., Ishizuka, O., Bogus, K. A., Gurnis, M., Hickey-Vargas, R., Aljahdali, M. H., Bandini-Maeder, A. N., Barth, A. P., Brandl, P. A., Drab, L., do Monte Guerra, R., Hamada, M., Jiang, F., Kanayama, K., Kender, S., Kusano, Y., Li, H., Loudin, L. C., Maffione, M., Marsaglia, K. M., McCarthy, A., Meffre, S., Morris, A., Neuhaus, M., Savov, I. P., Sena, C., Tepley III, F. J., van der Land, C., and Yogodzinski, Gene M. Zhang, Z.: A record of spontaneous subduction initiation in the Izu-Bonin-Mariana arc, Nature Geosci., 8, 728–733, https://doi.org/10.1038/ngeo2515, doi:10.1038/ngeo2515, 2015.

Baes, M. and Sobolev, S.: Mantle Flow as a Trigger for Subduction Initiation: A Missing Element of the Wilson Cycle Concept, Geochemistry, Geophysics, Geosystems, 18, 4469–4486, https://doi.org/10.1002/2017GC006962, http://dx.doi.org/10.1002/2017GC006962, 2017.

Behn, M. D., Lin, J., and Zuber, M. T.: Evidence for weak oceanic transform faults, Geophysical Research Letters, 29, 60–1–60–4, https://doi.org/10.1029/2002GL015612, https://agupubs.onlinelibrary.wiley.com/doi/abs/10.1029/2002GL015612, 2002.

Billen, M. and Gurnis, M.: Constraints on subducting plate strength within the Kermadec trench, J. Geophys. Res., 110, B05407, https://doi.org/10.1029/2004JB003308, doi:10.1029/2004JB003308, 2005.

Bloomer, S.: Distribution and origin of igneous rocks from the landward slopes of the Mariana Trench: Implications for its structure and evolution., J. Geophys. Res., 88, 7411–7428, 1983.

Bloomer, S. and Hawkins, J.: Petrology and geochemistry of boninite series volcanic rocks from the Mariana trench, Contrib. Mineral. Petrol., 97, 361–377, 1983.

Bonatti, E., Ligi, M., Borsetti, A., Gasperini, L., Negri, A., and Sartori, R.: Lower Cretaceous deposits trapped near the equatorial Mid-Atlantic Ridge, Nature, 380, 518–520, 1996.

Bousquet, R., Goffé, B., Henry, P., Le Pichon, X., and Chopin, C.: Kinematic, thermal and petrological model of the Central Alps: Lepontine metamorphism in the upper crust and eclogitisation of the lower crust, Tectonophysics, 273, 105–127, 1997.

Boutelier, D. and Beckett, D.: Initiation of Subduction Along Oceanic Transform Faults: Insights From Three-Dimensional Analog Modeling Experiments, Frontiers in Earth Science, 6, 204, https://doi.org/10.3389/feart.2018.00204, https://www.frontiersin.org/article/10.3389/feart.2018.00204, 2018.

Buffett, B.: Plate force du to bending at subduction zones, J. Geophys. Res., 111, B09405, https://doi.org/10.1029/2006JB004295, doi:10.1029/2006JB004295, 2006.

Byerlee, J.: Friction of rocks, Pure Appl. Geophys., 116, 615–626, 1978.

Cannat, M., Mamaloukas-Frangoulis, V., Auzende, J.-M., Bideau, D., Bonatti, E., Honnorez, J., Lagabrielle, Y., Malavieille, J., and Mevel, C.: A geological cross-section of the Vema fracture zone transverse ridge, Atlantic ocean, Journal of Geodynamics, 13, 97 – 117, https://doi.org/https://doi.org/10.1016/0264-3707(91)90034-C, http://www.sciencedirect.com/science/article/pii/026437079190034C, symposium Sy19- European Union of Geosciences Meeting, 1991.

Christensen, U. R.: An Eulerian technique for thermomechanical modeling, J. Geophys. Res., 97, 2015–2036, 1992.

Deschamps, A. and Lallemand, S.: The West Philippine Basin: a Paleocene-Oligocene backarc basin opened between two opposed subduction zones., J. Geophys. Res., 107, 2322, https://doi.org/10.1029/2001JB001706, 2002.

Deschamps, A. and Lallemand, S.: Geodynamic setting of Izu-Bonin-Mariana boninites, Geological Society, London, Special Publications,
5    219, 163–185, https://doi.org/10.1144/GSL.SP.2003.219.01.08, http://sp.lyellcollection.org/content/219/1/163, 2003.

Deschamps, A., Monié, P., Lallemand, S., Hsu, S.-K., and Yeh, J.: Evidence for Early Cretaceous oceanic crust trapped in the Philippine Sea Plate., Earth Planet. Sci. Lett., 179, 503–516, 2000.

Detrick, R. and Purdy, G.: The crustal structure of the Kane fracture zone from seismic refraction studies, J. Geophys. Res., 85, 3759–3777, 1980.

10   Dewandel, B., Lachassagne, P., and Qatan, A.: Spatial measurements of stream baseflow, a relevant method for aquifer characterization and permeability evaluation. Application to a hard-rock aquifer, the Oman ophiolite, Hydrological Processes, 18, 3391–3400, https://doi.org/10.1002/hyp.1502, https://onlinelibrary.wiley.com/doi/abs/10.1002/hyp.1502, 2004.

Doin, M.-P. and Henry, P.: Subduction initiation and continental crust recycling: the roles of rheology and eclogitization, Tectonophysics, 342, 163–191, 2001.

15   Doin, M.-P., Fleitout, L., and McKenzie, D.: Geoid anomalies and the structure of continental and oceanic lithospheres, J. Geophys. Res., 101, 16 119–16 135, 1996.

Doo, W.-B., Hsu, S.-K., Yeh, Y., Tsai, C., and Chang, C.: Age and tectonic evolution of the northwest corner of the West Philippine Basin, Mar. Geophys. Res., 36, 113–125, https://doi.org/10.1007/s11001-014-9234-8, 2015.

Duarte, J.-a. C., Rosas, F., Terrinha, P., Schellart, W. P., Boutelier, D., Gutscher, M., and Ribeiro, A.: Are subduction zones invading the
20   Atlantic? Evidence from the southwest Iberia margin, Geology, 41, 839–842, 2013.

Dumoulin, C., Doin, M.-P., and Fleitout, L.: Heat transport in stagnant lid convection with temperature- and pressure-dependent Newtonian or non-Newtonian rheology, J. Geophys. Res., 104, 12 759–12 778, 1999.

Dumoulin, C., Doin, M.-P., and Fleitout, L.: Numerical simulations of the cooling of an oceanic lithosphere above a convective mantle, Phys. Earth Planet. Inter., 125, 45–64, 2001.

25   Dymkova, D. and Gerya, T.: Porous fluid flow enables oceanic subduction initiation on Earth, Geophysical Research Letters, 40, 5671–5676, https://doi.org/10.1002/2013GL057798, http://dx.doi.org/10.1002/2013GL057798, 2013.

Eakin, D., McIntosh, K., Van Avendonk, H., and Lavier, L.: New geophysical constraints on a failed subduction initiation: The structure and potential evolution of the Gagua Ridge and Huatung Basin, Geochem. Geophys. Geosyst., 16, 1–21, 2015.

Escartìn, J. and Cannat, M.: Ultramafic exposures and the gravity signature of the lithosphere near the Fifteen-Twenty Fracture Zone (Mid-
30   Atlantic Ridge, 14$^o$-16.5$^o$N), Earth Planet. Sci. Lett., 171, 411–424, 1999.

Escartìn, J., Hirth, G., and Evans, B.: Nondilatant brittle deformation of serpentinites: Implications for Mohr-Coulomb theory and the strength of faults, J. Geophys. Res., 102, 2897–2913, 1997.

Farough, A., Moore, D. E., Lockner, D. A., and Lowell, R. P.: Evolution of fracture permeability of ultramafic rocks undergoing serpentinization at hydrothermal conditions: An experimental study, Geochemistry, Geophysics, Geosystems, 17, 44–55,
35   https://doi.org/10.1002/2015GC005973, https://agupubs.onlinelibrary.wiley.com/doi/abs/10.1002/2015GC005973, 2016.

Farrington, R. J., Moresi, L.-N., and Capitanio, F. A.: The role of viscoelasticity in subducting plates, Geochemistry, Geophysics, Geosystems, 15, 4291–4304, https://doi.org/10.1002/2014GC005507, https://agupubs.onlinelibrary.wiley.com/doi/abs/10.1002/2014GC005507, 2014.

Fournier, M., Chamot-Rooke, N., Rodriguez, M., Huchon, P., Petit, C., Beslier, M., and Zaragosi, S.: Owen Fracture Zone: The Arabia–India plate boundary unveiled, Earth Planet. Sci. Lett., 302, 247–252, 2011.

Fox, P. and Gallo, D.: A tectonic model for ridge-transition-ridge plate boundaries: Implications for the structure of oceanic lithosphere, Tectonophysics, 104, https://doi.org/10.1016/0040-1951(84)90124-0, 1983.

5  Fujiwara, T., Tamura, C., Nishizawa, A., Fujioka, K., Kobayashi, K., and Iwabuchi, Y.: Morphology and tectonics of the Yap Trench, Mar. Geophys. Res., 21, 69–86, 2000.

Gaina, C. and Müller, D.: Cenozoic tectonic and depth/age evolution of the Indonesian gateway and associated back-arc basins, Earth Sci. Rev., 83, 177–203, https://doi.org/10.1016/j.earscirev.2007.04.004, 2007.

Gerya, T., Connolly, J., and Yuen, D.: Why is terrestrial subduction one-sided?, Geology, 36, 43–46, 2008.

10  Godard, M., Luquot, L., Andreani, M., and Gouze, P.: Incipient hydration of mantle lithosphere at ridges: A reactive-percolation experiment, Earth and Planetary Science Letters, 371-372, 92 – 102, https://doi.org/https://doi.org/10.1016/j.epsl.2013.03.052, http://www.sciencedirect.com/science/article/pii/S0012821X13001799, 2013.

Gurnis, M., Hall, C., and Lavier, L.: Evolving force balance during incipient subduction, Geochem. Geophys. Geosyst., 5, Q07001, https://doi.org/10.1029/2003GC000681, doi:10.1029/2003GC000681, 2004.

15  Gutscher, M., Malod, J., Rehaul, J.-P., Contrucci, I., Klingelhoefer, F., Mendes-Victor, L., and Sparkman, W.: Evidence for active subduction beneath Gibraltar, Geology, 30, , 1071–1074, 2002.

Hall, C. and Gurnis, M.: Catastrophic initiation of subduction following forced convergence across fra ctures zones, Earth Planet. Sci. Lett., 212, 15–30, https://doi.org/10.1016/S0012-821X(03)00242-5, 2003.

Hall, C. E. and Gurnis, M.: Strength of fracture zones from their bathymetric and gravitational evolution, Journal of Geophysical Research:
20  Solid Earth, 110, https://doi.org/10.1029/2004JB003312, https://agupubs.onlinelibrary.wiley.com/doi/abs/10.1029/2004JB003312, 2005.

Hasterok, D.: A heat flow based cooling model for tectonic plates, Earth and Planetary Science Letters, 361, 34 – 43, https://doi.org/https://doi.org/10.1016/j.epsl.2012.10.036, http://www.sciencedirect.com/science/article/pii/S0012821X12006243, 2013.

Hawkins, J. and Batiza, R.: Metamorphic rocks of the Yap arc-trench system, Earth Planet. Sci. Lett., 37, 216–229, 1977.

Hegarty, K. A. and Weissel, J. K.: Complexities in the Development of the Caroline Plate Region, Western Equatorial Pacific, in:
25  The Ocean Basins and Margins, edited by Nairn, A., Stehli, F., and Uyeda, S., vol. 7B, pp. 277–301, Springer, Boston, MA, https://doi.org/https://doi.org/10.1007/978-1-4615-8041-6-6, 1988.

Hegarty, K. A., Weissel, J. K., and Hayes, D. E.: Convergence at the Caroline-Pacific Plate Boundary: Collision and Subduction, chap. 18, pp. 326–348, American Geophysical Union (AGU), https://doi.org/10.1029/GM027p0326, https://agupubs.onlinelibrary.wiley.com/doi/abs/10.1029/GM027p0326, 1983.

30  Hickey-Vargas, R., Yogodzinski, G., Ishizuka, O., McCarthy, A., Bizimis, M., Kusano, Y., Savov, I., and Arculus, R.: Origin of depleted basalts during subduction initiation and early development of the Izu-Bonin-Mariana island arc: Evidence from IODP expedition 351 site U1438, Amami-Sankaku basin, Geochem. Cosmochem. Acta, 229, 85–111, https://doi.org/doi.org/10.1016/j.gca.2018.03.007, 2018.

Hilde, T. and Lee, C.-S.: Origin and evolution of the west Philippine Basin: a new interpretation, Tectonophysics, 102, 85–104, 1984.

Hussong, D. and Uyeda, S.: Tectonic processes and the history of the Mariana Arc: a synthesis of the results of Deep Sea Drilling Project
35  Leg 60., Initial Rep Deep Sea Drill Proj, 60, 909–929, 1981.

Ishizuka, O., Kimura, J.-I., Li, Y. B., Stern, R. J., Reagan, M. K., Taylor, R. N., Ohara, Y., Bloomer, S. H., Ishii, T., Hargrove, U. S., and Haraguchi, S.: Early stages in the evolution of Izu-Bonin arc volcanism: New age, chemical, and isotopic constraints, Earth and Planetary

Science Letters, 250, 385 – 401, https://doi.org/https://doi.org/10.1016/j.epsl.2006.08.007, http://www.sciencedirect.com/science/article/pii/S0012821X06005772, 2006.

Ishizuka, O., Tani, K., Reagan, M. K., Kanayama, K., Umino, S., Harigane, Y., Sakamoto, I., Miyajima, Y., Yuasa, M., and Dunkley, D. J.: The timescales of subduction initiation and subsequent evolution of an oceanic island arc, Earth and Planetary Science Letters, 306, 229 – 240, https://doi.org/https://doi.org/10.1016/j.epsl.2011.04.006, http://www.sciencedirect.com/science/article/pii/S0012821X11002123, 2011.

Ishizuka, O., Taylor, R. N., Ohara, Y., and Yuasa, M.: Upwelling, rifting, and age-progressive magmatism from the Oki-Daito mantle plume, Geology, 41, 1011 – 1014, https://doi.org/https://doi.org/10.1130/G34525.1, 2013.

Ishizuka, O., Hickey-Vargas, R., Arculus, R. J., Yogodzinski, G. M., Savov, I. P., Kusano, Y., McCarthy, A., Brandl, P. A., and Sudo, M.: Age of Izu-Bonin-Mariana arc basement, Earth and Planetary Science Letters, 481, 80 – 90, https://doi.org/https://doi.org/10.1016/j.epsl.2017.10.023, http://www.sciencedirect.com/science/article/pii/S0012821X17305824, 2018.

Johnson, J. A., Hickey-Vargas, R., Fryer, P., Salters, V., and Reagan, M. K.: Geochemical and isotopic study of a plutonic suite and related early volcanic sequences in the southern Mariana forearc, Geochemistry, Geophysics, Geosystems, 15, 589–604, https://doi.org/10.1002/2013GC005053, https://agupubs.onlinelibrary.wiley.com/doi/abs/10.1002/2013GC005053, 2014.

Keenan, T. and Encarnación, J.: Unclear causes for subduction, Nature Geoscience, p. 338, https://doi.org/10.1038/ngeo2703, https://doi.org/10.1038/ngeo2703, 10.1038/ngeo2703, 2016.

Korenaga, J.: Scaling of plate tectonic convection with pseudoplastic rheology, Journal of Geophysical Research: Solid Earth, 115, n/a–n/a, https://doi.org/10.1029/2010JB007670, http://dx.doi.org/10.1029/2010JB007670, b11405, 2010.

Kuo, B.-Y., Chi, W.-C., Lin, C.-R., Chang, E.-Y., Collins, J., and Liu, C.-S.: Two-station measurement of Rayleigh wave phase velocities for the Huatung basin, the westernmost Philippine Sea, with OBS: implications for regional tectonics., Geophys. J. Int., 179, 1859–1869, https://doi.org/10.1111/j.1365-246X.2009.04391.x, 2009.

Lallemand, S.: High rates of arc consumption by subduction processes: Some consequences, Geology, 23, 551–554, 1995.

Lallemand, S.: Philippine Sea Plate inception, evolution and consumption with special emphasis on the early stages of Izu-Bonin-Mariana subduction, Progress in Earth and Planetary Science, 3, https://doi.org/10.1186/s40645-016-0085-6, 10.1186/s40645-016-0085-6, 2016.

Lebrun, J.-F., Lamarche, G., and Collot, J.-Y.: Subduction initiation at a strike-slip plate boundary: the Cenozoic Pacific-Australian plate boundary, south of New Zealand, Geophys. Res. Lett., 108, https://doi.org/10.1029/2002JB002041, 2003.

Leng, W. and Gurnis, M.: Subduction initiation at relic arcs, Geophys. Res. Lett., 42, 7014–7021, 2015.

Lu, G., Kaus, B. J. P., Zhao, L., and Zheng, T.: Self-consistent subduction initiation induced by mantle flow, Terra Nova, 27, https://doi.org/10.1111/ter.12140, https://doi.org/10.1111/ter.12140, 2015.

Mackwell, S., , Zimmerman, M., and Kohlstedt, D.: High-temperature deformation of dry diabase with applications to tectonics on Venus, J. Geophys. Res., 103, 975–984, 1998.

Maia, M., Sichel, S., Briais, A., Brunelli, D., Ligi, M., Ferreira, N., Campos, T., Mougel, B., Brehme, I., Hémond, C., Motoki, A., Moura, D., Scalabrin, C., Pessanha, I., Alves, E., Ayres, A., and Oliveira, P.: Extreme mantle uplift and exhumation along a transpressive transform fault, Nat. Geosci., https://doi.org/10.1038/NGEO2759, 2016.

Marques, F. and Kaus, B.: Speculations on the impact of catastrophic subduction initiation on the Earth System, Journal of Geodynamics, 93, 1 – 16, https://doi.org/http://dx.doi.org/10.1016/j.jog.2015.09.003, http://www.sciencedirect.com/science/article/pii/S0264370715300211, doi:10.1016/j.jog.2015.09.003, 2016.

Matsumoto, T. and Tomoda, Y.: Numerical simulation of the initiation of subduction at the fracture zone, J Phys Earth, 31, https://doi.org/10.4294/jpe1952.31.183, https://doi.org/10.4294/jpe1952.31.183, 1983.

Meckel, T., Mann, P., Mosher, S., and Coffin, M.: Influence of cumulative convergence on lithospheric thrust fault development and topography along the Australian-Pacific plate boundary south of New Zealand, Geochem. Geophys. Geosyst., 6, https://doi.org/10.1029/2005GC000914, 2005.

Moore, D., Lockner, D., Tanaka, H., and Iwata, K.: The coefficient of friction of chrysotile gouge at seismogenic depths, International Geology Review, 46, 385–398, 2004.

Morency, C. and Doin, M.-P.: Numerical simulations of the mantle delamination, J. Geophys. Res., 109, 3410, https://doi.org/10.1029/2003JB002414, doi:10.1029/2003JB002414, 2004.

Mortimer, N., Gans, P. B., Palin, J., Herzer, R. H., Pelletier, B., and M.Monzier: Eocene and Oligocene basins and ridges of the Coral Sea-New Caledonia region: Tectonic link between Melanesia, Fiji, and Zealandia, Tectonics, 33, 1386–1407, https://doi.org/10.1002/2014TC003598, 2014.

Natland, J. and Tarney, J.: Petrologic evolution of the Mariana Arc and back-arc basin system—a synthesis of drilling results in the South Philippine Sea, Initial Reports of the Deep Sea Drilling Project, 60, 877–908, https://ci.nii.ac.jp/naid/10026534957/en/, 1981.

Nikolaeva, K., Gerya, T. V., and Connolly, J. A.: Numerical modelling of crustal growth in intraoceanic volcanic arcs, Physics of the Earth and Planetary Interiors, 171, 336 – 356, https://doi.org/https://doi.org/10.1016/j.pepi.2008.06.026, http://www.sciencedirect.com/science/article/pii/S0031920108001556, recent Advances in Computational Geodynamics: Theory, Numerics and Applications, 2008.

Nikolaeva, K., Gerya, T. V., and Marques, F. O.: Subduction initiation at passive margins: numerical modeling, J Geophys Res, 115, https://doi.org/10.1029/2009JB006549, https://doi.org/10.1029/2009JB006549, 2010.

Patriat, M., Pichot, T., Westbrook, G., Umber, M., Deville, E., Bénard, F., Roest, W., Loubrieu, B., and the Antiplac cruise party: Evidence for Quaternary convergence between the North American and South American plates, east of the Lesser Antilles, Geology, 39(10), 2011.

Patriat, M., Collot, J., Danyushevsky, L., Fabre, M., Meffre, S., Falloon, T., Rouillard, P., Pelletier, B., Roach, M., and Fournier, M.: Propagation of back-arc extension into the arc lithosphere in the southern New Hebrides volcanic arc, Geochem. Geophys. Geosyst., 16, https://doi.org/10.1002/2015GC005717, 2015.

Pichot, T., Patriat, M., Westbrook, G., Nalpas, T., Gutscher, M., Roest, W., Deville, E., Moulin, M., Aslanian, D., and Rabineau, M.: The Cenozoic tectonostratigraphic evolution of the Barracuda Ridge and Tiburon Rise, at the western end of the North America–South America plate boundary zone, Mar. Geol., 303-306, 154–171, https://doi.org/10.1016/j.margeo.2012.02.001, 2012.

Quinquis, M., Buiter, S., and Ellis, S.: The role of boundary conditions in numerical models of subduction dynamics, Tectonophysics, 497, 57–70, 2011.

Raleigh, C. and Paterson, M.: Experimental deformation of serpentinite and its tectonic implications, J. Geophys. Res., 70, 3965–3985, 1965.

Ranalli, G.: Rheology of the Earth, Chapman and Hall, London, 2nd edn., 1995.

Reagan, M. K., Heaton, D. E., Schmitz, M. D., Pearce, J. A., Shervais, J. W., and Koppers, A. A.: Forearc ages reveal extensive short-lived and rapid seafloor spreading following subduction initiation, Earth and Planetary Science Letters, 506, 520 – 529, https://doi.org/https://doi.org/10.1016/j.epsl.2018.11.020, http://www.sciencedirect.com/science/article/pii/S0012821X18306794, 2019.

Ribe, N. and Christensen, U.: Three-dimensional modeling of plume-lithosphere interaction, J. Geophys. Res., 99, 699–682, 1994.

Rocchi, V., Sammonds, P. R., and Kilburn, C. R.: Flow and fracture maps for basaltic rock deformation at high temperatures, Journal of Volcanology and Geothermal Research, 120, 25 – 42, https://doi.org/https://doi.org/10.1016/S0377-0273(02)00343-8, http://www.sciencedirect.com/science/article/pii/S0377027302003438, 2003.

Sdrolias, M. and Müller, R.: Controls on back-arc basin formation, Geochem. Geophys. Geosyst., 7, https://doi.org/10.1029/2005GC001090, 2006.

Searle, R.: Multiple, closely spaced transform faults in fast-slipping fractures zones, Geology, 11, 1983.

Seton, M., Flament, N., Whittaker, J., Müller, R., Gurnis, M., and Bower, D.: Ridge subduction sparked reorganization of the Pacific plate-mantle system 60-50 million years ago, Geophys. Res. Lett., 42, https://doi.org/10.1002/2015GL063057, doi:10.1002/2015GL063057, 2015.

Sibuet, J.-C., Hsu, S.-K., Le Pichon, X., Le Formal, J.-P., Reed, D., Moore, G., and Liu, C.-S.: East Asia plate tectonics since 15 Ma: constraints from the Taiwan region, Tectonophysics, 344, 103–134, 2002.

Stern, R. and Bloomer, S.: Subduction zone infancy: examples from the Eocene Izu- Bonin-Mariana and Jurassic California arcs, Geol. Soc. Am. Bull., 104, 1621–1636, 1992.

Stern, R. J. and Gerya, T.: Subduction initiation in nature and models: A review, Tectonophysics, https://doi.org/10.1016/j.tecto.2017.10.014, https://doi.org/10.1016/j.tecto.2017.10.014, 2018.

Tesei, T., Harbord, C. W. A., De Paola, N., Collettini, C., and Viti, C.: Friction of Mineralogically Controlled Serpentinites and Implications for Fault Weakness, Journal of Geophysical Research: Solid Earth, 123, 6976–6991, https://doi.org/10.1029/2018JB016058, https://agupubs.onlinelibrary.wiley.com/doi/abs/10.1029/2018JB016058, 2018.

Tetreault, J. L. and Buiter, S. J. H.: Future accreted terranes: a compilation of island arcs, oceanic plateaus, submarine ridges, seamounts, and continental fragments, Solid Earth, 5, 1243–1275, https://doi.org/10.5194/se-5-1243-2014, https://www.solid-earth.net/5/1243/2014/, 2014.

Thielmann, M. and Kaus, B. J. P.: Shear heating induced lithospheric-scale localization: does it result in subduction?, Earth Planet Sci Lett, 359/360, https://doi.org/10.1016/j.epsl.2012.10.002, https://doi.org/10.1016/j.epsl.2012.10.002, 2012.

Tortella, D., Torne, M., and Perez-Estaun, A.: Geodynamic Evolution of the Eastern Segment of the Azores-Gibraltar Zone: The Gorringe Bank and the Gulf of Cadiz Region, Mar. Geophys. Res., 19, 211 – 230, 1997.

Turcotte, D. and Schubert, G.: Geodynamics: Applications of continuum physics to geological problems, Cambridge University Press, New York, second edn., 1982.

Uyeda, S. and Kanamori, H.: Back-arc opening and the mode of subduction zones, J. Geophys. Res., 84, 1049–1062, 1979.

van Keken, P., King, S., Schmeling, H., Christensen, U., Neumeister, D., and Doin, M.-P.: A comparison of methods for the modeling of thermochemical convection, J. Geophys. Res., 102, 22 477–22 495, 1997.

Violay, M., Gibert, B., Mainprice, D., Evans, B., Dautria, J.-M., Azais, P., and Pezard, P.: An experimental study of the brittle-ductile transition of basalt at oceanic crust pressure and temperature conditions, Journal of Geophysical Research: Solid Earth, 117, https://doi.org/10.1029/2011JB008884, https://agupubs.onlinelibrary.wiley.com/doi/abs/10.1029/2011JB008884, 2012.

Whattam, S. A. and Stern, R. J.: Late Cretaceous plume-induced subduction initiation along the southern margin of the Caribbean and NW South America: The first documented example with implications for the onset of plate tectonics, Gondwana Research, 27, 38 – 63, https://doi.org/http://dx.doi.org/10.1016/j.gr.2014.07.011, http://www.sciencedirect.com/science/article/pii/S1342937X14002391, 2015.

Wilks, K. and Carter, N.: Rheology of some continental lower crustal rocks, Tectonophysics, 182, 57–77, 1990.

Wolfson-Schwehr, M., Boettcher, M. S., McGuire, J. J., and Collins, J. A.: The relationship between seismicity and fault structure on the Discovery transform fault, East Pacific Rise, Geochem. Geophys. Geosyst., 15, 3698–3712, https://doi.org/10.1002/2014GC005445, https://agupubs.onlinelibrary.wiley.com/doi/abs/10.1002/2014GC005445, 2014.

Yongsheng, Z., Changrong, H., Xiaoge, H., Juan, S., Zunan, S., and Hua, K.: Rheological Complexity of Mafic Rocks and Effect of Mineral Component on Creep of Rocks, Earth Science Frontiers, 16, 76–87, 2009.

Zhou, X., Li, Z.-H., Gerya, T. V., Stern, R. J., Xu, Z., and Zhangi, J.: Subduction initiation dynamics along a transform fault control trench curvature and ophiolite ages, Geology, 46, 607–610, https://doi.org/https://doi.org/10.1130/G40154.1, 2018.

5  Zhu, G., Gerya, T. V., Yuen, D. A., Honda, S., Yoshida, T., and Connolly, J. A. D.: Three-dimensional dynamics of hydrous thermal-chemical plumes in oceanic subduction zones, Geochemistry, Geophysics, Geosystems, 10, https://doi.org/10.1029/2009GC002625, https://agupubs.onlinelibrary.wiley.com/doi/abs/10.1029/2009GC002625, 2009.

Zhu, G., Gerya, T. V., Honda, S., Tackley, P. J., and Yuen, D. A.: Influences of the buoyancy of partially molten rock on 3-D plume patterns and melt productivity above retreating slabs, Physics of the Earth and Planetary Interiors, 185, 112 – 121,
10  https://doi.org/https://doi.org/10.1016/j.pepi.2011.02.005, http://www.sciencedirect.com/science/article/pii/S0031920111000392, 2011.

**Table 1.** Oceanic TFs or FZs where potential subduction initiated during Cenozoic times.

| Regions | Relative age of the downgoing plate at initiation | Age inception at initiation (Ma) | Age range of downgoing plate\upper plate (Ma) | Stress state at initiation | Present state (convergence length since initiation) | Observations | Sources |
|---|---|---|---|---|---|---|---|
| Izu-Bonin-Mariana | older | 52-50? | 40-65?\0-2? | unknown | mature subduction (> 1000 km?) | presence of remnant arcs nearby TF in upper plate | 1, 2, 3 |
| Yap | older | 20? | 15-10?\10-5? | unknown | subduction (150 km?) | possible collision ? | 4, 5, 6, 7 |
| Matthew & Hunter | older | 1.8 | 28\0-10? | thrusting | subduction initiation | Loyalty Ridge collision →new spreading center =Eissen Ridge + lateral propagation of NH subduction | 8, 9 |
| Mussau | older | 1 | 35-100?\30? | thrusting | no subduction/incipient? | variation in convergence rate at eastern boundary of Caroline plate | 10 |
| Macquarie | older | 6 | 27?\20? | thrusting | no subduction/incipient? | transpressive relay | 11, 12 |
| Romanche | older | 40-35? | 80?\30? | thrusting | no subduction | transpressive relay | 13 |
| Hjort | younger | 11-6? | 2-5?\15-27? | thrusting | subduction initiation (100 km?) | $v_c = 0.7$–$2.7$ cm/yr, convergence obliquity=45-80° | 14, 15 |
| Gagua | younger | 50-24? | 5-25?\125-100? | probably transpressive | aborted subduction | change in plates kinematics or jump of subduction? | 16, 17, 18, 19, 20, 21, 22 |
| Barracuda | younger | 2.3 | <73\73 | slight compression | vertical motion only (1.2 km uplift - 0.8 km subsidence) | consequence of relative motion between South and North America plates? | 23, 24 |
| Tiburon | younger | 11.6 | ≥73\≥73 | slight compression | no subduction | ridge rise by 1km +1.5 km of subsidence | 23, 24 |
| Gorringe | unknown | 40-10 ? | >100\ >100 | transpressive | small and distributed | consequence of plates reorganization | 25, 26, 27 |
| Saint Paul | unknown | 11 | 0-5?\0-5? | transpressive | no subduction | plates motion change | 28 |
| Owen | unknown | 20 | 40 ?\ ?? | strike-slip | no subduction - vertical motion only | restraining bend along an oceanic strike-slip plate boundary | 29 |

References: 1- Stern and Bloomer (1992); 2-Lallemand (2016); 3-Sdrolias and Müller (2006) ; 4-Gaina and Müller (2007); 5-Fujiwara et al. (2000); 6-Hawkins and Batiza (1977); 7-Hegarty and Weissel (1988); 8-Patriat et al. (2015); 9-Mortimer et al. (2014); 10-Hegarty et al. (1983); 11-Lebrun et al. (2003); 12-Meckel et al. (2005); 13-Bonatti et al. (1996); 14-Meckel et al. (2005); 15-Deschamps and Lallemand (2002); 16-Abecassis et al. (2016); 17-Deschamps et al. (2000); 18-Sibuet et al. (2002); 19-Hilde and Lee (1984); 20-Doo et al. (2015); 21-Kuo et al. (2009); 22-Eakin et al. (2015); 23-Patriat et al. (2011); 24-Pichot et al. (2012); 25-Gutscher et al. (2002); 26-Duarte et al. (2013); 27-Tortella et al. (1997); 28-Maia et al. (2016); 29-Fournier et al. (2011).

**Table 2.** Constant names and values.

| Parameter name | Symbol | Value |
|---|---|---|
| Box height | $H_0$ | 555 km |
| Bottom temperature | $T_b$ | 1888 K |
| Surface temperature | $T_s$ | 273 K |
| Mantle density at surface | $\rho_m$ | 3300 kg.m$^{-3}$ |
| Mantle radiogenic heat production | $D_0$ | $9.20 \times 10^{-8}$ W.m$^{-3}$ |
| Adiabatic gradient | $\left(\frac{\partial T}{\partial z}\right)_{adiab}$ | 0.45 K.km$^{-1}$ |
| Thermal diffusivity | $\kappa$ | $8 \times 10^{-7}$ m$^2$.s$^{-1}$ |
| Thermal expansion coefficient | $\alpha$ | $3.5 \times 10^{-5}$ K$^{-1}$ |
| Heat capacity | $C_p$ | $0.971 \times 10^3$ J.(K.kg)$^{-1}$ |
| Activation energy for the mantle | $E_a^m$ | 465 kJ/mol |
| Activation volume | $V_a$ | $1.7 \times 10^{-5}$ m$^3$/mol |
| Pre-exponential factor in non-Newtonian rheology | $B_0$ | 339428.7 MPa$^{-3}$.s$^{-1}$ |
| Dissipation number | $Di = \frac{\alpha g H_0}{C_p}$ | 0.196 |
| Gravity acceleration | $g$ | 9.81 m.s$^{-2}$ |
| Oceanic crust thickness | $h_c$ | 8.3 km |
| Cohesive strength at $z = 0$ | $C_0$ | 1 MPa |
| Stress exponent in the brittle rheology | $n_p$ | 30 |
| Stress exponent in the dislocation creep rheology | $n$ | 3 |
| Gas constant | $R$ | 8.314 J.(mol. K)$^{-1}$ |
| Reference strain rate | $\dot{\varepsilon}_{ref}$ | $10^{-14}$ s$^{-1}$ |
| Reference viscosity at box bottom | $\nu_{BB}$ | $3.94 \times 10^{20}$ Pa.s |

Table 3: List of simulations quoted in the text. See the Supplementary data for the complete simulation list.

| Run | $A_y$vs$A_o$ (Myr, Myr) | $\gamma_{TF}/\gamma_c$ or $\gamma_c$[1] | $\gamma_m$ | $\rho_c/\rho_{TF}$[2] (kg.m$^{-3}$) | $E_a^c$ (kJ/ mol) | $L_w$[3] $(A_y; A_o)$ (km;km) | Specific test | Bottom boundary condition | Result |
|---|---|---|---|---|---|---|---|---|---|
| S1a | 0vs2 | 0.0005 | 1.6 | 3300 | 360 | 1100 | - | open | OPS-mode 2 |
| S1b | 0vs2 | 0.05 | 1.6 | 3300 | 360 | 0 | - | open | YPVSI |
| S1c | 0vs2 | 0.05 | 1.6 | 3300 | 185 | 0 | - | open | YP dripping |
| S2a | 0vs5 | 0.0005 | 1.6 | 3300 | 360 | 1100 | - | open | OPS-mode 2 |
| S2b | 0vs5 | 0.0005 | 0.05 | 3300 | 360 | 1100 | - | open | OPS-mode 2 |
| S11a | 0vs100 | 0.0005 | 1.6 | 3300 | 360 | 1100 | - | open | OPS-mode 1 |
| S14e | 2vs5 | 0.05 | 1.6 | 3300 | 185 | 0 | - | open | OPS-mode 2, SB |
| S14i | 2vs5 | 0.0005 | 1.6 | 3300 | 360 | 17;42 | - | open | OPS-mode 2 |
| S14n | 2vs5 | 0.0005/0.05 | 1.6 | 2920/3300 | 360 | 50 | - | closed | Double SI |
| S14t | 2vs5 | 0.0005/0.01 | 0.8 | 3160/3160 | 360 | 50 | - | closed | Close to OPS |
| S15b | 2vs10 | 0.0005 | 1.6 | 3300 | 360 | 1100 | - | open | OPS-mode 2 |
| S15g | 2vs10 | 0.05 | 1.6 | 2920/3300 | 185 | 1100 | - | closed | YPVSI |
| S15h | 2vs10 | 0.05 | 1.6 | 2920/3300 | 360 | 1100 | $\Delta T_p = 250^o$C | open | YPSI |
| S15j | 2vs10 | 0.0005/0.01 | 0.8 | 3160/3300 | 360 | 50 | - | closed | OPS-mode 2 |
| S15k | 2vs10 | 0.0005/0.01 | 0.8 | 3160/3160 | 360 | 50 | - | closed | Close to OPS |
| S16a | 2v20 | 0.0005/0.05 | 1.6 | 3300 | 360 | 50 | - | closed | Close to OPS |
| S16b | 2v20 | 0.0005/0.05 | 1.6 | 2920/3300 | 360 | 50 | - | closed | Heavy YPS |
| S16c | 2v20 | 0.0005/0.05 | 1.6 | 2920/2920 | 360 | TF only[4] | - | closed | YP retreat |
| S16d | 2v20 | 0.0005/0.05 | 1.6 | 2920/3300 | 360 | 50 | - | closed | Heavy YPS |
| S16f | 2vs20 | 0.0005/0.01 | 0.6 | 3160/3160 | 360 | 50 | - | closed | OPS-mode 2 |
| S16g | 2vs20 | 0.05/0.05 | 1.6 | 2920/3330 | 360 | 50 | - | closed | YP shortening |
| S16h | 2vs20 | 0.0005/0.01 | 0.8 | 3160/3160 | 360 | 50 | - | closed | OPS-mode 2 |
| S17c | 2vs40 | 0.0005 | 1.6 | 3300 | 360 | 1100 | - | open | OPS-mode 2 |
| S17f | 2vs40 | 0.05 | 1.6 | 3300 | 185 | 0 | - | open | YP dripping |
| S17n | 2vs40 | 0.0005 | 1.6 | 3300 | 360 | TF only[4] | - | closed | OPS-mode 2 |
| S17o | 2vs40 | 0.0005/0.05 | 1.6 | 3300 | 360 | 50 | - | closed | YPVSI |
| S17t | 2vs40 | 0.0005/0.01 | 0.6 | 3160/3160 | 360 | 50 | - | closed | OPS-mode 2 |
| S17u | 2vs40 | 0.05/0.0005 | 1.6 | 3300 | 360 | TF only[4] | - | closed | YPS |
| S17w | 2vs40 | 0.0005/0.01 | 0.8 | 3160/3160 | 360 | 50 | - | closed | OPS-mode 2 |
| S18c | 2vs80 | 0.005 | 1.6 | 3300 | 360 | 1100 | - | open | cooling |
| S18d | 2vs80 | 0.0007 | 1.6 | 3300 | 360 | 1100 | - | open | OPS-mode 2 |
| S18e | 2vs80 | 0.001 | 1.6 | 3300 | 360 | 1100 | - | open | OPS-mode 2 |

. . . continued

| Run | $A_y, A_o$ | $\gamma_{TF}/\gamma_c$ | $\gamma_m$ | $\rho_c/\rho_{TF}$ | $E_a^c$ | $L_w$ ($A_y$; $A_o$) | Test | Bottom BC | Result |
|---|---|---|---|---|---|---|---|---|---|
| S18p | 2vs80 | 0.0005 | 0.6 | 2920/3300 | 360 | TF only[4] | - | closed | OPS-mode 2 |
| S22j | 5vs15 | 0.0005 | 0.1 | 3300 | 360 | 1100 | - | open | OPS-mode 2+SB |
| S22k | 5vs15 | 0.0005 | 0.05 | 3300 | 360 | 1100 | - | open | OPS-mode 2+SB |
| S25a | 5vs35 | 0.0005 | 1.6 | 3300 | 360 | 1100 | - | open | Close to OPS |
| S27c | 5vs50 | 0.0005 | 1.6 | 3300 | 360 | 42;260 | - | open | OPS-mode 1 |
| S29a | 5vs120 | 0.0005 | 1.6 | 3300 | 360 | 0 | - | open | Close to OPS |
| S34a | 7vs80 | 0.0005 | 1.6 | 3300 | 360 | 1100 | - | open | Close to OPS |
| S36b | 10vs20 | 0.0005/0.05 | 1.6 | 2920/2920 | 360 | TF only[4] | - | closed | YPS |
| S37c | 10vs40 | 0.0005 | 0.4 | 3300 | 360 | 1100 | - | open | cooling |
| S37d | 10vs40 | 0.0005 | 0.1 | 3300 | 360 | 1100 | - | open | Close to OPS |
| S37e | 10vs40 | 0.0005 | 0.075 | 3300 | 360 | 1100 | - | open | Close to OPS |
| S37f | 10vs40 | 0.0005 | 0.05 | 3300 | 360 | 1100 | - | open | OPS-mode 1 |
| S37x | 10vs40 | 0.0005/0.05 | 0.05 | 2920/3300 | 360 | TF only[4] | - | closed | cooling |
| S38a | 10vs50 | 0.0005 | 0.1 | 3300 | 360 | 1100 | - | open | OPS-mode 1 |
| S41a | 10vs100 | 0.0005 | 1.6 | 3300 | 360 | 1100 | - | open | cooling |
| S43a | 10vs140 | 0.0005 | 1.6 | 3300 | 360 | 1100 | - | open | Close to OPS |
| S44a | 10vs150 | 0.0005 | 1.6 | 3300 | 360 | 1100 | - | open | Close to OPS |
| S47a | 15vs60 | 0.0005 | 0.1 | 3300 | 360 | 1100 | - | open | OPS-mode 1 |
| S47b | 15vs60 | 0.0005 | 0.08 | 3300 | 360 | 1100 | - | open | OPS-mode 1 |
| S47c | 15vs60 | 0.0005 | 0.06 | 3300 | 360 | 1100 | - | open | OPS-mode 1 |
| S47d | 15vs60 | 0.0005 | 0.05 | 3300 | 360 | 1100 | - | open | OPS-mode 1 |
| S49g | 20vs40 | 0.0005 | 0.05 | 3300 | 360 | 1100 | - | open | cooling |
| S49h | 20vs40 | 0.0005 | 0.005 | 3300 | 360 | 1100 | - | open | OPS, SB, YPD |
| S51a | 20vs80 | 0.0005 | 1.6 | 3300 | 360 | 1100 | - | open | cooling |
| S51b | 20vs80 | 0.0005 | 0.1 | 3300 | 360 | 1100 | - | open | Close to OPS |
| S51c | 20vs80 | 0.0005 | 0.08 | 3300 | 360 | 1100 | - | open | Close to OPS |
| S51d | 20vs80 | 0.0005 | 0.06 | 3300 | 360 | 1100 | - | open | OPS-mode 1 |
| S51e | 20vs80 | 0.0005 | 0.05 | 3300 | 360 | 1100 | - | open | OPS-mode 1 |
| S51f | 20vs80 | 0.0005/0.05 | 1.6 | 3300 | 360 | 50 | - | closed | cooling |
| S57a | 25vs100 | 0.0005 | 0.05 | 3300 | 360 | 1100 | - | open | OPS-mode 1 |
| S57b | 25vs100 | 0.0005 | 0.075 | 3300 | 360 | 1100 | - | open | Close to OPS |

[1] If one value only is indicated, the oceanic crust (3) in Fig. 2 is assumed to have the same brittle parameter as the weak material forming domains (1) and (2). [2] If only one value indicated, then $\rho_c = \rho_{TF}$. [3] When one value only is indicated, $L_w$ is identical on both plates. [4] The weak material is imposed at the fault zone (1) only (Fig. 2). "tw": thermal transition width at the plate boundary. $\Delta T_p$: temperature anomaly

within the plume head. $\nu_{ref}$: reference viscosity at the lithosphere-asthenosphere boundary ($2.74 \times 10^{19}$ Pa.s). OPS: older plate sinking. YPVSI: YP vertical subduction initiation (as in Fig. 5-6). YP retreat: backward drift of the younger plate, as sketched in Fig. 4-3. YPs: younger plate sinking, as sketched in Fig. 4-4b. Double SI: double subduction initiation (as in Fig. 4-5). Heavy YPS: subduction of the heavy YP segment, as illustrated in Fig. 4-4a. SB: slab break-off. YPD: young plate detachment from the surface and sinking into the mantle.